A Primal Formulation for Imposing Periodic Boundary Conditions on Conforming and Nonconforming Meshes

Sunday C. Aduloju [a], Timothy J. Truster [a] †

[a] Department of Civil and Environmental Engineering, University of Tennessee, Knoxville, 318 John D. Tickle
Engineering Building, Knoxville, TN 37996

Computer Methods in Applied Mechanics and Engineering

Abstract

A variational multiscale Discontinuous Galerkin (VMDG) method is developed for microscale modeling of domains containing conforming and non-conforming meshes. Essentially, the product of the applied volume-average strain (or macro-strain) and the domain diameter acts as an imposed displacement jump within the VMDG terms. Hence, the method is suitable for modeling deformation of both block and truly (self) periodic representative volume elements (RVEs). The primal displacement field and macro-strain are the only unknowns because the method eliminates the Lagrange multiplier (LM) enforcement of the kinematic constraint. Rigorous derivation of the method provides a framework to accommodate either the macro-stress or macro-strain as the driver of the microscale boundary value problem. The method is developed first for finite deformations and then specialized to small deformation kinematics. Algorithmic modifications to the method are also studied for their effects on tangent symmetry and convergence rate. The results from numerical studies for isotropic and anisotropic materials show that the proposed method is robust, accurate, stable and variationally consistent for modeling complicated conforming and nonconforming RVEs.

Key Words: Variational multiscale method, Discontinuous Galerkin, Periodic boundary conditions, Finite strains, RVE

---

† Assistant Professor. Corresponding author: Ph: (865) 974-1913; Fax: (865) 974-2669, e-mail: ttruster@utk.edu

1. Introduction

Fundamental understanding of microscale deformation mechanisms continues to be pursued for advanced materials and heterogeneous systems that are designed for aerospace vehicles. These heterogeneous materials such as fibrous composites and metallic alloys have complex dependence on spatial distribution, size, texture and shape of different constituents. The need to define the macroscopic mechanical response of heterogenous materials has led to past and present development of homogenization techniques.

The analytical techniques [1-4] traditionally used to predict the collective response of multi-phase materials have been found to be ill-suited for microscale modeling of materials subjected to large deformations and non-uniform cyclic loading. The application of analytical techniques is also usually hindered by the complex geometry of the representative microstructure [5, 6]. Computational homogenization is a preferred alternative because of its accuracy in accounting for the non-linear characteristics of a material at the microscale, and the method is not constrained by the geometry of the domain of interest [5, 7-10]. Though the technique is computationally expensive, it offers an established procedure for obtaining the effective properties of a heterogenous material [4, 5, 11].

Commonly in computational homogenization, the primary macroscopic kinematical quantities such as the deformation gradient enter the microscale boundary value problem (BVP) through the boundary constraints on the representative volume element (RVE). Typical kinematic constraint types are the linear displacement boundary condition, constant traction boundary condition, and periodic boundary condition (PBC) [5, 6, 12, 13]. Among the three constraints, the PBC is widely used and considered more efficient for modeling of the underlying microstructure because the predicted results converge faster to the effective properties of RVE as size increases [5, 7, 8, 13-15].

The Lagrange multiplier (LM) method [16, 17] is commonly used for enforcing PBC on the RVE through the imposition of identical displacement fields on two matching nodes on opposite boundaries. The limitation of the method lies in the non-suitability of the method for RVE containing non-conforming meshes, also termed as non-periodic meshes. Since RVEs meshes are generated often directly from microstructure images which inherently produce non-periodic meshes, a recent LM approach employs weak enforcement of PBC instead of pointwise constraints [18]. However, this method belongs to the category of mixed field problems for which stability can be a concern [19, 20], and the extra LM degrees of freedom must be determined with the displacement solution. Also, the LM field is required to belong to a mortar space or modified trace space to enforce an orthogonality relationship with the displacement jump [21]. The extra degrees of freedom could be reduced by relying on either the biorthogonality condition that localizes the coupling conditions to construct dual Lagrange multiplier shape functions [21-23] or the static condensation method [9, 24, 25]. Non-periodic surfaces have also been treated using LM by discretizing the boundary surface independently for smooth transitioning of micro-macro BVP in [12]. Another LM [26] approach enforces quasi-periodic boundary conditions on nonconforming meshes using shape functions to interpolate the displacement field between nodes on the master and slave opposing surfaces of the RVE. Other means of enforcing PBC such as the surface-to-surface constraint [27] which largely depends on the choice of master and slave surfaces may not be robust, and the method of the unidirectional polynomial interpolation of the displacement fields [8, 28] could require very high order polynomial interpolation functions.

The Discontinuous Galerkin (DG) method is a popular method for weakly enforcing continuity of solution fields across naturally or artificially disjointed surfaces [29-33]. The DG method has been described as a promising method for enforcing PBC on RVE boundaries in scalar field problems [34], and subsequently employed to treat the higher-order continuity requirements of the macroscale problem for a second order computational homogenization scheme [35]. To the best knowledge of the authors, this paper presents for the first time the development of Discontinuous Galerkin method for the microscale problem of the first order computational homogenization scheme of solid mechanics. This paper discusses the variational multiscale Discontinuous Galerkin (VMDG) method earlier applied in a continuum context for small and large strains [36-40].

The VMDG method is suitable for enforcing PBC on microstructures containing periodic and non-periodic meshes. While the existing methods generally only permit the macro-strain to drive the RVE boundary conditions, the rigorous derivation of the VMDG method provides a framework to accommodate either the macro-stress or macro-strain on the microscale boundary value problem. Macro-stress driven problems are appropriate for performing patch tests and convergence studies of the method and also for cases where displacement and traction conditions are specified, such as unconfined uniaxial tension. The VMDG method is a single field formulation that is free from stability concerns associated with mixed formulations like the mortar-type Lagrange multiplier method. The consistently-derived stabilizing terms require no calibration and account for element geometry and material properties along the boundary. Hence, the method is suitable for modeling deformation of both block and truly (self) periodic RVEs. As shown in Figure 1 (a), for block RVE the domain boundary cuts through geometric features such as grains or fibers. In the latter case for truly periodic RVEs in Figure 1 (b), the RVE boundary conforms to the geometric features, which can ease the mesh generation of quality element shapes and aspect ratios. Instead of focusing on only small or finite deformations, the VMDG method is developed in the finite deformation context and subsequently specialized to small deformation of RVEs. Contrary to earlier presentations in the literature that usually start from the weak form or minimization form [8, 16, 18], this paper begins from the strong form of a microscale problem to derive from a LM formulation to an underlying stabilized DG method by reliance on variational multiscale (VMS) ideas.

The organization of the paper is as follows. We begin in Section 2 by giving a brief summary of the essentials of the microscale problem and PBC enforcement at the RVE boundaries as well as describing the governing equations and associated weak form of the Lagrange multiplier formulation. In Section 3, we describe the derivation which relies on variational multiscale ideas (VMS) for the stabilized formulation for enforcing PBC. The algorithmic modifications of the VMDG method are proposed in Section 4, and specialization of the VMDG formulation to RVE undergoing small deformation are briefly discussed in Section 5. In Section 6, multiple benchmark problems for error convergence analysis and method consistency tests for 2-D and 3-D microstructures are performed. Finally, we give concluding remarks in Section 7.

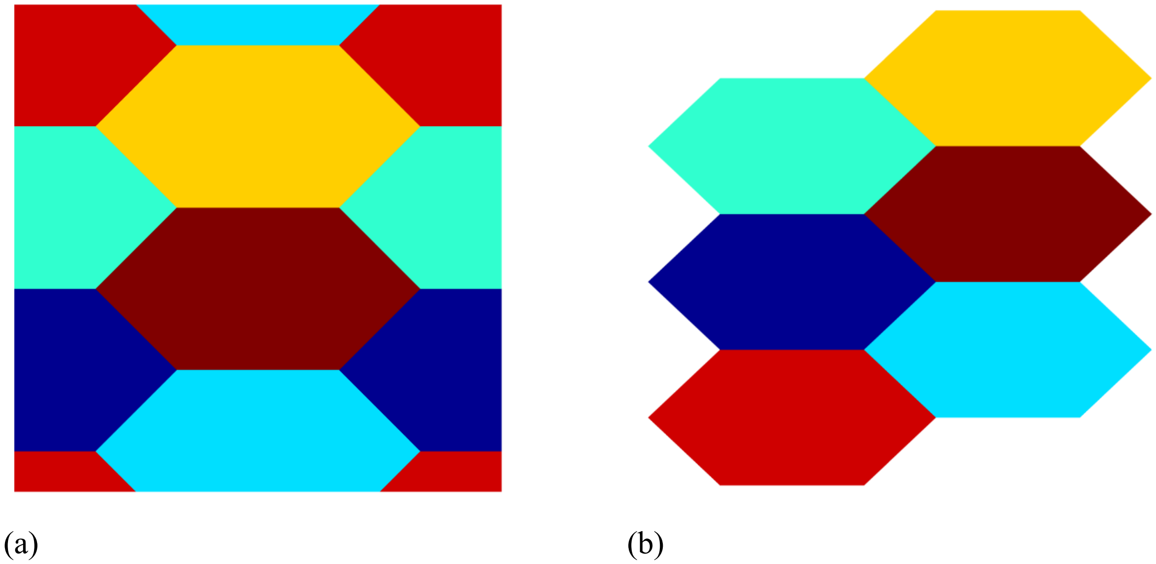
(a) (b)

Figure 1. RVE instantiations: (a) 2D block RVE; (b) 2D truly (self) periodic RVE

2. Microscale Modeling and Periodic Boundary Condition for RVE

To motivate the formulation of the periodic VMDG method, we recall key concepts from mechanical multiscale theory [15]. This section begins by describing the kinematic fields in the context of the microscale region termed as a representative volume element (RVE) domain. Next, the principle of scale separation is summarized as a means to link the deformation of constituents at the microscale with the average deformation and stress experienced at the macroscale, followed by the Hill-Mandel principle for energetic consistency as well as classes of kinematically admissible boundary conditions for the microscale problem. Lastly, the strong form and weak form are posed for the microscale problem with periodic boundary conditions, which is the focus of the VMDG derivations in Section 3.

2.1. Microscale domain and kinematics

Let $\Omega \subset \mathbb{R}^{n_{\mathrm{sd}}}$ be an open bounded RVE domain with piecewise periodic boundary Γ, where $n_{sd} \geq 2$ is the number of spatial dimensions. The boundary Γ is divided into two subsets $\Gamma^{+} = \bigcup_{i} \Gamma_{i}^{+}$ and $\Gamma^{-} = \bigcup_{i} \Gamma_{i}^{-}$, where i denotes an RVE boundary pair, and the subsets satisfy $\Gamma^{+} \cup \Gamma^{-} = \Gamma$; see Figure 2. The RVE is deformed according to the motion $\boldsymbol{\phi}(\boldsymbol{X},t)$ which maps the points $\boldsymbol{X} \in \Omega$ in the reference configuration to points $\boldsymbol{x} = \boldsymbol{\phi}(\boldsymbol{X},t)$ in the current configuration. The displacement $\boldsymbol{u}(\boldsymbol{X},t) = \boldsymbol{\phi}(\boldsymbol{X},t) - \boldsymbol{X}$ is the difference between the locations in the current configuration and reference configuration while the deformation gradient $\boldsymbol{F}$ is defined as follows:

$$\boldsymbol{F}(\boldsymbol{X},t) = \frac{\partial \boldsymbol{x}}{\partial \boldsymbol{X}} = \mathrm{GRAD}\, \boldsymbol{x} \tag{1}$$

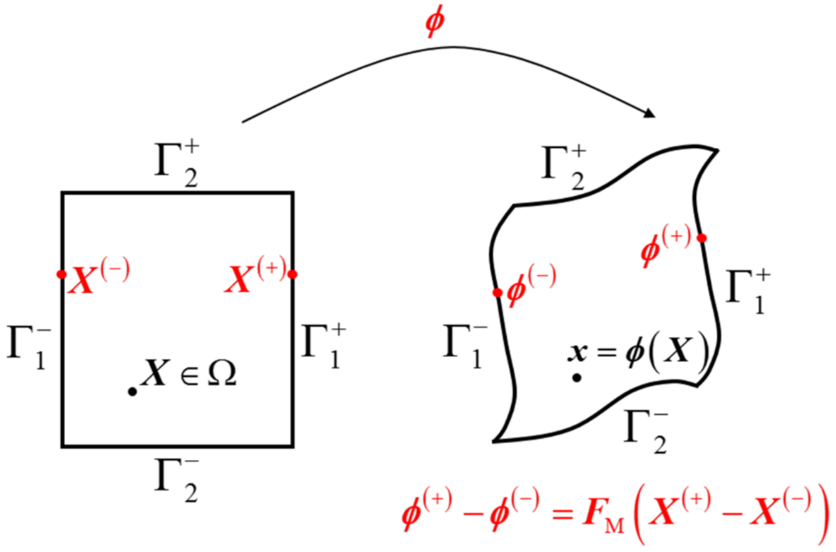

Figure 2. The deformation of the RVE from reference to current configurations

2.2. Physical scale separation principles

The concept of scale separation relies on the existence of an RVE associated to a material point $\boldsymbol{X}_{\mathrm{M}} \in \Omega_{\mathrm{M}}$ in the macroscale, as depicted in Figure 3, which has a characteristic length that is small compared to the continuum scale.

$$\boldsymbol{\phi}(\boldsymbol{X}) = \boldsymbol{F}_{\mathrm{M}}\,\boldsymbol{X} + \widehat{\boldsymbol{\phi}} \tag{2}$$

$$\boldsymbol{F}(\boldsymbol{X},t) = \boldsymbol{F}_{\mathrm{M}} + \mathrm{GRAD}\,\widehat{\boldsymbol{\phi}} \tag{3}$$

The microscopic deformation map $\boldsymbol{\phi}$ can be decomposed into a linear mapping $\boldsymbol{F}_{\mathrm{M}}\,\boldsymbol{X}$ and a deformation mapping fluctuation $\widehat{\boldsymbol{\phi}}$ according to (2). Thus, the microscale deformation gradient in (1) can also be expressed in terms of the macroscale deformation gradient as in (3).

Macro-to-micro coupling of the kinematical constraint in physical scale separation usually requires the assumption that the volume average of the microscale deformation gradient is equal to the volume average of the microscale deformation gradient.

$$\boldsymbol{F}_{\mathrm{M}}\left(\boldsymbol{X}_{\mathrm{M}}\right)=\frac{1}{V_0}\int_{\Omega}\boldsymbol{F}\left(\boldsymbol{X}\right)\mathrm{d}\Omega \tag{4}$$

where $\boldsymbol{X}\in\Omega$ and V_0 is the microscale domain volume. Evaluating the volume average of the microscale gradient (3) simplifies as follows after applying the divergence theorem on the second term:

$$\frac{1}{V_0}\int_{\Omega}\boldsymbol{F}\left(\boldsymbol{X}\right)\mathrm{d}\Omega=\boldsymbol{F}_{\mathrm{M}}\left(\boldsymbol{X}_{\mathrm{M}}\right)+\frac{1}{V_0}\int_{\Omega}\mathrm{GRAD}\,\widehat{\boldsymbol{\phi}}\,\mathrm{d}\Omega=\boldsymbol{F}_{\mathrm{M}}\left(\boldsymbol{X}_{\mathrm{M}}\right)+\frac{1}{V_0}\int_{\Gamma}\widehat{\boldsymbol{\phi}}\otimes\boldsymbol{N}\,\mathrm{d}\Gamma \tag{5}$$

where $\boldsymbol{N}$ is the outward unit normal. By comparing (4) and (5), it is observed that the surface integral of the mapping fluctuation field must vanish, and several options for enforcing this condition are mentioned subsequently.

The equally important Hill-Mandel principle [18, 41, 42] is also employed to satisfy macro-to-micro energetic consistency by defining the volume average of the microscopic deformation energy to be equivalent to the macroscopic energy, where the δ terms signify variational strains:

$$\boldsymbol{P}_{\mathrm{M}}\left(\boldsymbol{X}_{\mathrm{M}}\right):\delta\boldsymbol{F}_{\mathrm{M}}\left(\boldsymbol{X}_{\mathrm{M}}\right)=\frac{1}{V_0}\int_{\Omega}\boldsymbol{P}\left(\boldsymbol{X}\right):\delta\boldsymbol{F}\left(\boldsymbol{X}\right)\mathrm{d}\Omega \tag{6}$$

The fulfillment of the Hill-Mandel principle holds if and only if there is no work due to external surface traction and body force of the RVE:

$$\int_{\Gamma}\boldsymbol{\eta}_o\cdot\boldsymbol{t}\,\mathrm{d}\Gamma=0,\qquad\int_{\Omega}\boldsymbol{\eta}_o\cdot\boldsymbol{b}\,\mathrm{d}\Omega=0 \tag{7}$$

$$\frac{1}{V_0}\int_{\Omega}\boldsymbol{P}\left(\boldsymbol{X}\right):\delta\boldsymbol{F}\left(\boldsymbol{X}\right)\mathrm{d}\Omega=\left(\frac{1}{V_0}\int_{\Gamma}\boldsymbol{N}\cdot\boldsymbol{P}\left(\boldsymbol{X}\right)\otimes\boldsymbol{X}\mathrm{d}\Gamma\right):\delta\boldsymbol{F}_{\mathrm{M}}+\frac{1}{V_0}\int_{\Gamma}\boldsymbol{N}\cdot\boldsymbol{P}\left(\boldsymbol{X}\right)\cdot\delta\widehat{\boldsymbol{\phi}}\mathrm{d}\Gamma \tag{8}$$

According to [15], it has been shown that the right hand of (6) can be expressed as (8). Since the contribution of the mapping fluctuation field vanishes, the macroscopic first Piola-Kirchhoff (PK) stress tensor $\boldsymbol{P}_{\mathrm{M}}\left(\boldsymbol{X}_{\mathrm{M}}\right)$ is equal to the volume average of the microscopic counterpart $\boldsymbol{P}\left(\boldsymbol{X}\right)$:

$$\boldsymbol{P}_{\mathrm{M}}=\frac{1}{V_0}\int_{\Gamma}\boldsymbol{N}\cdot\boldsymbol{P}\left(\boldsymbol{X}\right)\otimes\boldsymbol{X}\mathrm{d}\Gamma=\frac{1}{V_0}\int_{\Omega}\boldsymbol{P}\left(\boldsymbol{X}\right)\mathrm{d}\Omega \tag{9}$$

The reader is referred to [15] for details of the derivation of the average theory.

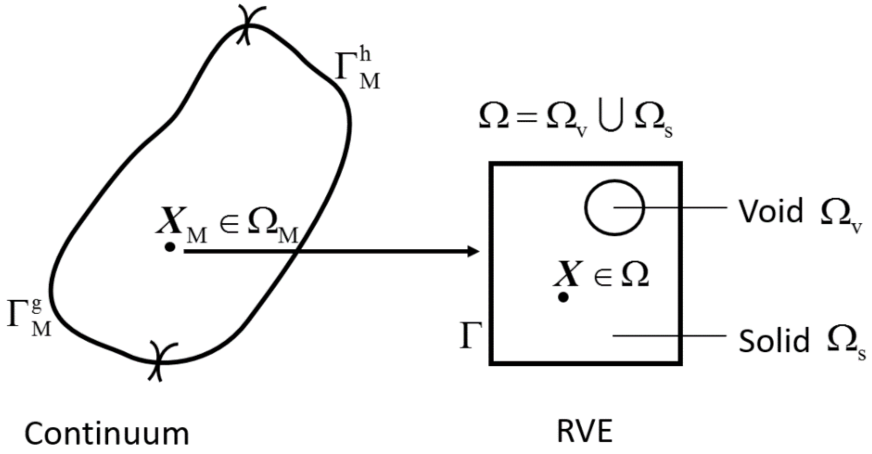

Figure 3. An RVE domain Ω residing at the vicinity of $\boldsymbol{X}_{\mathrm{M}}\in\Omega_{\mathrm{M}}$ at the continuum scale

Several methods exist to fulfill the condition whereby the mapping fluctuation field vanishes. The *Taylor (Voigt)* model simply assumes no fluctuations exists in the RVE volume such that it experiences an identically constant strain. The *Sachs (Reuss)* model assumes an identically constant stress in the RVE volume. The Taylor model generally produces a stiff estimate of the macroscopic overall mechanical response while the Sachs model produces a very compliant estimate. Although both models are computationally inexpensive and provide rough estimates, they do not simultaneously capture both equilibrium and compatibility of the microscale phases. The *minimal kinematic boundary condition* requires the boundary integral of the fluctuations on the boundary expressed in (5) to vanish. The *uniform displacement boundary condition* assumes that there is no fluctuation at the RVE boundary and the displacements at the RVE boundary are prescribed according to macroscopic deformation gradient. The uniform traction boundary condition allows the traction on the RVE boundary to be prescribed according to the macroscopic stress. The uniform displacement boundary condition overestimates the macroscopic effective stiffness, while both the minimal kinematic condition and the uniform traction condition underestimate the macroscopic effective stiffness.

The *periodic boundary condition* is suitable for RVE with geometrically periodic boundary Γ which is divided into two subsets $\Gamma^{+} = \bigcup_{i} \Gamma_{i}^{+}$ and $\Gamma^{-} = \bigcup_{i} \Gamma_{i}^{-}$, where i denotes an RVE boundary pair. The microscopic deformation map $\boldsymbol{\phi}$ on the RVE boundary can be expressed by (2) with counterparts at two opposite boundaries of the RVE in Figure 2 (b). The key kinematical assumption is the periodicity of the fluctuation $\widehat{\boldsymbol{\phi}}$ along Γ to ensure displacement compatibility:

$$\boldsymbol{P}_{\mathrm{M}} = \frac{1}{V_0} \int_{\Gamma} \boldsymbol{N} \cdot \boldsymbol{P}(\boldsymbol{X}) \otimes \boldsymbol{X} \mathrm{d}\Gamma = \frac{1}{V_0} \int_{\Omega} \boldsymbol{P}(\boldsymbol{X}) \mathrm{d}\Omega \tag{10}$$

Herein, we consider Γ^{+} as the primary side and refer to points on Γ^{-} through the pairwise operator $\wp$ in Figure 4; the treatment of rectangular and non-rectangular RVE is systematic using these pairwise maps as discussed in [42]. The periodic boundary condition is widely used and considered more efficient for modeling of the underlying microstructure because the predicted results converge faster to the effective properties of RVE as size increases [5, 7, 8, 13, 14].

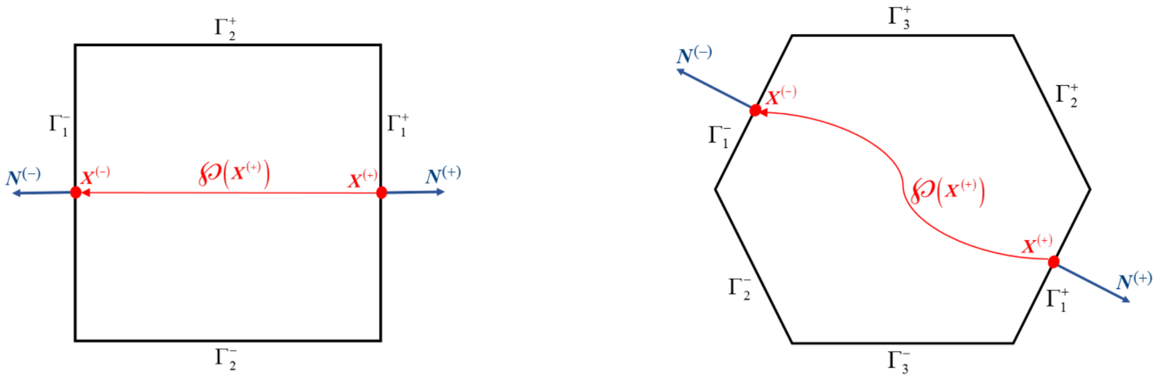

(a) (b)

Figure 4. Pairwise mapping of boundary quantities for (a) rectangular RVE and (b) hexagonal RVE

2.3. Microscale governing equations and weak form

Adopting PBC for the kinematic constraint, the strong form of the microscale boundary value problem is posed as:

$$\mathrm{DIV}\,\boldsymbol{P}\left(\boldsymbol{F}\right)=\boldsymbol{0} \qquad \text{in} \quad \Omega \tag{11}$$

$$[\![\boldsymbol{\phi}]\!]=\boldsymbol{F}_{\mathrm{M}}[\![\boldsymbol{X}]\!] \qquad \text{on} \;\; \Gamma^{+} \tag{12}$$

$$\boldsymbol{P}\left(\boldsymbol{X}^{(+)}\right)\boldsymbol{N}^{(+)}=\boldsymbol{\lambda}\left(\boldsymbol{X}^{(+)}\right)=-\boldsymbol{P}\left(\wp\left(\boldsymbol{X}^{(+)}\right)\right)\boldsymbol{N}^{(-)} \qquad \text{on}\;\Gamma^{+} \tag{13}$$

$$\int_{\Gamma^{+}}\boldsymbol{\lambda}\otimes[\![\boldsymbol{X}]\!]\mathrm{d}\Gamma=V_{0}\boldsymbol{P}_{\mathrm{M}} \tag{14}$$

The momentum balance equation (11) of the microscale domain is defined only in terms of the divergence of the first PK stress tensor according to the Hill-Mandel principle. The deformation jump $[\![\boldsymbol{\phi}]\!]$ along Γ^{+} is constrained by the macroscale deformation gradient $\boldsymbol{F}_{\mathrm{M}}$ according to (12) which derives from the decomposition (2) and the periodicity (10) conditions. Throughout, the vector valued jump operator is defined as $[\![\bullet]\!]=(\bullet)^{(+)}-(\bullet)^{(-)}$. This constraint (12) is imposed through the Lagrange multiplier (LM) field $\boldsymbol{\lambda}$ in (13) which also enforces the equilibrium of the tractions along the RVE boundary. Finally, the prescribed macroscale stress $\boldsymbol{P}_{\mathrm{M}}$ transmits to the RVE surface according to (14).

Note that both $\boldsymbol{F}_{\mathrm{M}}$ and $\boldsymbol{P}_{\mathrm{M}}$ belong to the space of second order tensors that can be described in component form as the space $\mathcal{T}=\otimes_{j=1}^{n_{\mathrm{sd}}}\mathbb{R}^{n_{\mathrm{sd}}}$ with dimension $n_{\mathrm{sd}}\times n_{\mathrm{sd}}$ once a coordinate system is specified. For a well-posed problem, exactly $n_{\mathrm{sd}}\times n_{\mathrm{sd}}$ tensor components amongst the total $2\left(n_{\mathrm{sd}}\times n_{\mathrm{sd}}\right)$ strain and stress components can be prescribed within (12) and (14) while the remaining components are unknowns along with $\boldsymbol{\phi}$ and $\boldsymbol{\lambda}$. We denote these prescribed values as $\left\{\bar{F}_M\right\}_{j=1}^{n_F}$ and $\left\{\bar{P}_M\right\}_{j=1}^{n_P}$ with $n_F + n_P = n_{\mathrm{sd}} \times n_{\mathrm{sd}}$.

Remark:

The distinguishing feature of this BVP compared to the strong forms underlying our previous VMDG developments are the non-zero displacement jump (12) *and the surface integral of the tractions* (14). *In fact, for macro-stress driven problems when* $\boldsymbol{P}_{\mathrm{M}}$ *is prescribed, then the macro-strain* $\boldsymbol{F}_{\mathrm{M}}$ *becomes an unknown that is solved for alongside the deformation field. Aspects of representing this unknown in the discrete setting are discussed in Section 3.3 and the Appendix.*

Subsequently, the governing equations (11) and (13) are multiplied by weighting function $\boldsymbol{\eta}_o$, integrated over their respective regions, and the divergence theorem is applied. Similarly, equation (12) is multiplied by weighting function $\boldsymbol{\mu}$, (14) is multiplied by a weighting tensor $\boldsymbol{\kappa}$, and (12) is integrated over Γ^+. Thus, the weak form of the microscale problem is expressed as: Find $\{\boldsymbol{\phi}, \boldsymbol{\lambda}, \boldsymbol{F}_{\mathrm{M}}\} \in \mathcal{S} \times \mathcal{Q} \times \mathcal{T}_F$ such that for all $\{\boldsymbol{\eta}_o, \boldsymbol{\mu}, \boldsymbol{\kappa}\} \in \mathcal{S} \times \mathcal{Q} \times \mathcal{T}_0$:

$$\int_\Omega \mathrm{GRAD}\, \boldsymbol{\eta}_o : \boldsymbol{P}\, \mathrm{d}V - \int_{\Gamma^+} \boldsymbol{\lambda} \cdot [\![\boldsymbol{\eta}_o]\!]\, \mathrm{d}A = 0 \tag{15}$$

$$-\int_{\Gamma^+} \boldsymbol{\mu} \cdot \left([\![\boldsymbol{\phi}]\!] - \boldsymbol{F}_{\mathrm{M}} [\![\boldsymbol{X}]\!] \right) \mathrm{d}A = 0 \tag{16}$$

$$-\int_{\Gamma^+} \left(\boldsymbol{\kappa} [\![\boldsymbol{X}]\!] \right) \cdot \left(\boldsymbol{\lambda} - \boldsymbol{P}_{\mathrm{M}} \boldsymbol{N}^{(+)} \right) \mathrm{d}A = 0 \tag{17}$$

The appropriate functional spaces for the functions in the weak form are expressed as (18) – (21):

$$\mathcal{S} = \left\{ \boldsymbol{\phi} \middle| \boldsymbol{\phi} \in \left[H^1(\Omega) \right]^{n_{\mathrm{sd}}},\ \det\left(\boldsymbol{F}(\boldsymbol{\phi}) \right) > 0 \right\} \tag{18}$$

$$\mathcal{Q} = \left\{ \boldsymbol{\lambda} \middle| \boldsymbol{\lambda} \in \left[H^{-\frac{1}{2}}(\Gamma_{\mathrm{I}}) \right]^{n_{\mathrm{sd}}} \right\} \tag{19}$$

$$\mathcal{T}_F = \left\{ \boldsymbol{F}_M \,\middle|\, \boldsymbol{F}_M \in \mathcal{T}, F_{M,j} = \bar{F}_{M,j} \text{ for } j = 1 \text{ to } n_F \right\} \tag{20}$$

$$\mathcal{T}_0 = \left\{ \boldsymbol{\kappa} \,\middle|\, \boldsymbol{\kappa} \in \mathcal{T}, \kappa_j = 0 \text{ for } j = 1 \text{ to } n_F \right\} \tag{21}$$

where $H^1(\Omega)$ and $H^{-\frac{1}{2}}$ are standard Sobolev spaces. Notice that the integration of the surface terms in (15) – (17) is performed on Γ^+ only, which is an outcome of the node pair mapping $\wp$ that identifies a unique $\boldsymbol{X}^{(-)}$ for each $\boldsymbol{X}^{(+)}$. For example, the conversion between one term in (17) and (14) proceeds as follows:

$$\int_{\Gamma^+} \left(\boldsymbol{\kappa}[\![\boldsymbol{X}]\!]\right)\cdot\left(\boldsymbol{P}_\mathrm{M}\boldsymbol{N}^{(+)}\right)\mathrm{d}\Gamma = \int_{\Gamma} \left(\boldsymbol{\kappa}\boldsymbol{X}\right)\cdot\left(\boldsymbol{P}_\mathrm{M}\boldsymbol{N}\right)\mathrm{d}\Gamma = \mathrm{tr}\left[\boldsymbol{P}_M^T\boldsymbol{\kappa}\int_{\Omega}\nabla\boldsymbol{X}\,\mathrm{d}\Omega\right] = V_0\boldsymbol{P}_\mathrm{M}:\boldsymbol{\kappa} \tag{22}$$

This surface mapping is not limited to rectangular RVE in Figure 4(a) but could be carefully performed on hexagonal shaped RVE as in Figure 4(b) and on irregular and complex 3-D RVE domains; see examples in [43] and Section 6.4 herein. Also, while the definition of the interface jump depends on the ordering of the boundaries as in [36], the final weak form obtained at the completion of the derivations is independent of the ordering.

For completeness, we remark that the weak form in the case of hyperelastic materials ($\boldsymbol{P}(\boldsymbol{F}) = \partial W/\partial\boldsymbol{F}$) can be shown to be equivalent to the saddle point of the following functional:

$$\int_{\Omega} W(\boldsymbol{F})\,\mathrm{d}\Omega - \int_{\Gamma^+}\left(\boldsymbol{\lambda}\otimes\boldsymbol{N}^{(+)}\right):\left(\underline{[\![\boldsymbol{\phi}]\!]} - \boldsymbol{F}_\mathrm{M}\underline{[\![\boldsymbol{X}]\!]}\right)\mathrm{d}\Gamma - \int_{\Gamma^+}\boldsymbol{P}_\mathrm{M}:\left(\boldsymbol{F}_\mathrm{M}\underline{[\![\boldsymbol{X}]\!]}\right)\mathrm{d}\Gamma \tag{23}$$

where $\underline{[\![\bullet]\!]} = (\bullet)^{(+)}\otimes\boldsymbol{N}^{(+)} + (\bullet)^{(-)}\otimes\boldsymbol{N}^{(-)}$ is the tensorial jump operator.

3. Multiscale decomposition

The weak form (15) – (17) has been solved traditionally using a collocation approach for the LM field (i.e. multi-point constraints of paired nodes), but this is possible only if the discretization of Γ is periodic. In general, the mixed weak form (15) – (17) has two main drawbacks: it requires solving for an additional unknown LM field, and the discretized form must satisfy the Babuska-Brezzi condition [44, 45] to avoid stability issues, the latter being difficult for non-periodic meshes.

In the steps that follow, the LM formulation is converted to the single-field formulation with enhanced stability by systematically condensing out $\boldsymbol{\lambda}$ using variational multiscale ideas [46-48]. Although the key concepts in the context of small and large deformations can be found in our previous works [36, 37, 40, 49], the additional terms from enforcing the PBC (12) motivate us to revisit both the fine-scale models and the coarse-scale embedding.

An overlapping decomposition into coarse and fine scales is assumed within the microscale BVP of the deformation map $\boldsymbol{\phi}$ and weighting function $\boldsymbol{\eta}_o$ within the RVE:

$$\boldsymbol{\phi} = \tilde{\boldsymbol{\phi}} \circ \hat{\boldsymbol{\phi}}, \qquad \boldsymbol{\eta}_o = \tilde{\boldsymbol{\eta}}_o + \hat{\boldsymbol{\eta}}_o \tag{24}$$

where $\circ$ denotes the composition of mapping functions between the fine scale deformation $\tilde{\boldsymbol{\phi}}$ and the coarse scale deformation $\hat{\boldsymbol{\phi}}$. The coarse-scale deformation map $\hat{\boldsymbol{\phi}}$ is associated to the discrete function space and the fine scale $\tilde{\boldsymbol{\phi}}$ can be considered as the error filtered out by the finite element mesh. The weighting functions $\hat{\boldsymbol{\eta}}_o$ and $\tilde{\boldsymbol{\eta}}_o$ are associated with the coarse and fine scales. The linearity of the weak form (15) – (17) with respect to $\boldsymbol{\eta}_o$ enables the separation into a coarse-scale problem (25) – (27) and a fine-scale problem (28):

Coarse-scale problem

$$\hat{R}\left(\hat{\boldsymbol{\eta}}_o;\hat{\boldsymbol{\phi}},\tilde{\boldsymbol{\phi}},\boldsymbol{\lambda}\right) = \int_\Omega \mathrm{GRAD}\,\hat{\boldsymbol{\eta}}_o : \boldsymbol{P}\mathrm{d}V - \int_{\Gamma^+} \boldsymbol{\lambda}\cdot[\![\hat{\boldsymbol{\eta}}_o]\!]\,\mathrm{d}A - \int_{\Gamma^+} \boldsymbol{\kappa}[\![\boldsymbol{X}]\!]\cdot\left(\boldsymbol{\lambda} - \boldsymbol{P}_\mathrm{M}\boldsymbol{N}^{(+)}\right)\mathrm{d}A = 0 \tag{25}$$

$$\hat{R}_{\boldsymbol{\kappa}}\left(\boldsymbol{\kappa};\boldsymbol{\lambda}\right) = -\int_{\Gamma^+} \boldsymbol{\kappa}[\![\boldsymbol{X}]\!]\cdot\left(\boldsymbol{\lambda} - \boldsymbol{P}_\mathrm{M}\boldsymbol{N}^{(+)}\right)\mathrm{d}A = 0 \tag{26}$$

$$\hat{R}_{\mu}\left(\boldsymbol{\mu},\hat{\boldsymbol{\phi}},\tilde{\boldsymbol{\phi}},\boldsymbol{F}_\mathrm{M}\right) = -\int_{\Gamma^+} \boldsymbol{\mu}\cdot\left([\![\tilde{\boldsymbol{\phi}}\circ\hat{\boldsymbol{\phi}}]\!] - \boldsymbol{F}_\mathrm{M}[\![\boldsymbol{X}]\!]\right)\mathrm{d}A = 0 \tag{27}$$

Fine-scale problem

$$\tilde{R}\left(\tilde{\boldsymbol{\eta}}_o;\hat{\boldsymbol{\phi}},\tilde{\boldsymbol{\phi}},\boldsymbol{\lambda}\right) = \int_\Omega \mathrm{GRAD}\,\tilde{\boldsymbol{\eta}}_o : \boldsymbol{P}^{(\alpha)}\mathrm{d}V - \int_{\Gamma^+} \boldsymbol{\lambda}\cdot[\![\tilde{\boldsymbol{\eta}}_o]\!]\,\mathrm{d}A = 0 \tag{28}$$

3.1. Modeling of fine scales

It is worth mentioning that the fine-scale problem in (28) produced from the multiscale decomposition of the microscale weak form is similar to those in our previous VMDG interface formulations for compatible and equilibrated domains [40] and weak and strong discontinuities [37]. Namely, in [50], a body force is included and the surface integral is over an interface rather than Γ^{+}. Although these earlier formulations were applied in a continuum setting, the versatility of the VMDG method is manifested by the similarity of the fine-scale equations for the microscale problem. Hence, the fine-scale modeling details translate directly from [50], and we summarize the three key steps leading to the analytical fine-scale solution.

First, the coarse-scale fields are discretized using finite elements Ω_e to cover Ω. The fine-scale fields are assumed to be localized only within the elements adjoining Γ and approximated using sufficiently higher-order edge bubble functions b_s over the sectors $\omega_s \subseteq \Omega_e$ such that it satisfies the requisite property for vanishing along all sector edges except the boundary segment $\gamma_s \subset \Gamma$ [36]. A complete listing of b_s for two and three dimensional element shapes is given in [51]. The bubble functions effectively localize (28) into a series of problems posed over pairs of conforming sectors; namely, the sectors are chosen such that each point $\boldsymbol{X}^{(+)} \in \gamma_s^{+} \subset \text{closure}\left(\omega_s^{+}\right)$ has an image $\boldsymbol{X}^{(-)} = \wp\left(\boldsymbol{X}^{(+)}\right) \in \gamma_s^{-} \subset \text{closure}\left(\omega_s^{-}\right)$ where the sectors lie within single elements Ω_e^{+} and Ω_e^{-}. The segments are disjoint, and their unions cover Γ^{+} and Γ^{-}; see the useful illustrations in [50].

Second, the fine scales are treated as a small perturbation such that $\tilde{\boldsymbol{\phi}} \circ \hat{\boldsymbol{\phi}} \simeq \hat{\boldsymbol{\phi}} + \Delta\tilde{\boldsymbol{u}}$, and the fine-scale problem is linearized to facilitate the substitution of the edge bubble functions and an analytical solution. The linearized weak form is expressed in terms of the acoustic tensor

$\mathbf{A}^{(\alpha)}\left(\boldsymbol{F}^{(\alpha)}\right)$ of the material moduli given in (29) as well as [37, 40, 51, 52], where the superscript α takes the value $+$ or $-$ on the boundary Γ^{+} and Γ^{-}, respectively. A detailed discussion of the linearization procedure that exposes the geometric and material nonlinearity within the acoustic tensor can be found in [47].

$$\mathbf{A}^{(\alpha)}\left(\boldsymbol{F}^{(\alpha)}\right)=\frac{\partial^{2}W^{(\alpha)}}{\partial\boldsymbol{F}\partial\boldsymbol{F}} \tag{29}$$

Third, we solve for the fine-scale field in terms of the coarse scales fields $\hat{\boldsymbol{\phi}}$ and $\boldsymbol{\lambda}$ and assume that the fine-scale bubble function is orthogonal to the coarse-scale residual by neglecting the interior residual terms. The resulting fine-scale solution on either boundary is as follows:

$$\Delta\tilde{\boldsymbol{u}}^{(+)}=\boldsymbol{\tau}_{s}^{(+)}\cdot\left[-\boldsymbol{\lambda}-\boldsymbol{P}^{(+)}\cdot\boldsymbol{N}^{(+)}\right],\qquad \Delta\tilde{\boldsymbol{u}}^{(-)}=\boldsymbol{\tau}_{s}^{(-)}\cdot\left[\boldsymbol{\lambda}-\boldsymbol{P}^{(-)}\cdot\boldsymbol{N}^{(-)}\right] \tag{30}$$

where

$$\boldsymbol{\tau}_{s}^{(\alpha)}=\left[\operatorname{meas}\left(\gamma_{s}\right)\right]^{-1}\left(\int_{\gamma_{s}}b_{s}^{(\alpha)}\,\mathrm{d}A\right)^{2}\tilde{\boldsymbol{\tau}}_{s}^{(\alpha)} \tag{31}$$

$$\tilde{\boldsymbol{\tau}}_{s}^{(\alpha)}=\left[\int_{\omega_{s}^{(\alpha)}}\mathrm{GRAD}\,\boldsymbol{b}_{s}^{(\alpha)}:\mathbf{A}^{(\alpha)}:\mathrm{GRAD}\,\boldsymbol{b}_{s}^{(\alpha)}\,\mathrm{d}V\right]^{-1} \tag{32}$$

These three assumptions enable the analytical representation of the fine scales in terms of the boundary residual on either side of the periodic domain according to (30), in a manner similar to the development of stabilized finite element formulations [48, 53-55]. Hence, the stability tensor $\boldsymbol{\tau}_{s}^{(\alpha)}$ that scales the residual is not a free tuning parameter but rather emerges from the consistent derivation, where the tensor depends on the element size, element shape, polynomial order and the acoustic tensor of the material.

3.2. Variational embedding into the coarse-scale problem

Recall that the fine-scale field is small and localized only at the adjoining interface. Therefore, the deformation jump operator can be linearized as $\left[\!\left[\tilde{\boldsymbol{\phi}}\circ\hat{\boldsymbol{\phi}}\right]\!\right]\simeq\left[\!\left[\hat{\boldsymbol{\phi}}\right]\!\right]+\left[\!\left[\Delta\tilde{\boldsymbol{u}}\right]\!\right]$ according to [40].

Substituting this linearization along with the fine-scale solution (30) into the continuity equation (16) produces (33).

$$-\int_{\Gamma^+} \boldsymbol{\mu} \cdot \left[[\![\hat{\boldsymbol{\phi}}]\!] - \boldsymbol{\tau}_s^{(+)} \cdot \left(\boldsymbol{\lambda} - \boldsymbol{P}^{(+)} \cdot \boldsymbol{N}^{(+)} \right) + \boldsymbol{\tau}_s^{(-)} \cdot \left(-\boldsymbol{\lambda} - \boldsymbol{P}^{(-)} \cdot \boldsymbol{N}^{(-)} \right) - \boldsymbol{F}_{\mathrm{M}} [\![\boldsymbol{X}]\!] \right] \mathrm{d}A = 0 \tag{33}$$

Because of the enhanced stability derived from the fine-scale model, this expression can be solved pointwise by selecting the Lagrange multiplier space $\mathcal{Q}$ to encompass all L_2 functions on Γ^+, resulting in a locally defined expression on each segment γ_s that is a function of the weighted average traction.

$$\boldsymbol{\lambda} = \{ \boldsymbol{P} \cdot \boldsymbol{N} \} + \boldsymbol{\tau}_s \cdot \left([\![\hat{\boldsymbol{\phi}}]\!] - \boldsymbol{F}_{\mathrm{M}} [\![\boldsymbol{X}]\!] \right) \tag{34}$$

$$\{ (\bullet) \cdot \boldsymbol{N} \} = \boldsymbol{\delta}_s^{(+)} \cdot (\bullet)^{(+)} \cdot \boldsymbol{N}^{(+)} - \boldsymbol{\delta}_s^{(-)} \cdot (\bullet)^{(-)} \cdot \boldsymbol{N}^{(-)} \tag{35}$$

The flux weighting tensor $\boldsymbol{\delta}_s^{(\alpha)} = \boldsymbol{\tau}_s \cdot \boldsymbol{\tau}_s^{(\alpha)}$ and stability tensor $\boldsymbol{\tau}_s = \left(\boldsymbol{\tau}_s^{(+)} + \boldsymbol{\tau}_s^{(-)} \right)^{-1}$ are expressed in terms of $\boldsymbol{\tau}_s^{(\alpha)}$ and thus inherit the dependency on the element configuration and material properties. A distinguishing feature of (34) compared to previous VMDG methods is that the Lagrange multiplier field is driven by the macroscale deformation gradient $\boldsymbol{F}_{\mathrm{M}}$.

The expression (34) is substituted into (30), and both are placed within the coarse-scale equilibrium equation (25). Simplifying the result along the lines of [50], these steps yield a modified coarse-scale problem (36) that is stable and is free from the additional LM field.

Modified coarse-scale problem

$$\begin{aligned} R(\boldsymbol{\eta}_o, \boldsymbol{\kappa}; \boldsymbol{\phi}, \boldsymbol{F}_{\mathrm{M}}) = {} & \int_\Omega \mathrm{GRAD}\, \boldsymbol{\eta}_o : \boldsymbol{P}\, \mathrm{d}V - \int_{\Gamma^+} \boldsymbol{\kappa} [\![\boldsymbol{X}]\!] \cdot \boldsymbol{P}_{\mathrm{M}} \boldsymbol{N}^{(+)} \mathrm{d}A \\ & + \int_{\Gamma^+} \left[[\![\boldsymbol{\eta}_o]\!] - \boldsymbol{\kappa} [\![\boldsymbol{X}]\!] \right] \cdot \boldsymbol{\tau}_s \cdot \left([\![\boldsymbol{\phi}]\!] - \boldsymbol{F}_{\mathrm{M}} [\![\boldsymbol{X}]\!] \right) \mathrm{d}A \\ & - \int_{\Gamma^+} \left[[\![\boldsymbol{\eta}_o]\!] - \boldsymbol{\kappa} [\![\boldsymbol{X}]\!] \right] \cdot \{ \boldsymbol{P} \cdot \boldsymbol{N} \}\, \mathrm{d}A \\ & - \int_{\Gamma^+} \{ (\mathrm{GRAD}\, \boldsymbol{\eta}_o : \mathbf{A}) \cdot \boldsymbol{N} \} \cdot \left([\![\boldsymbol{\phi}]\!] - \boldsymbol{F}_{\mathrm{M}} [\![\boldsymbol{X}]\!] \right) \mathrm{d}A \\ & - \int_{\Gamma^+} [\![(\mathrm{GRAD}\, \boldsymbol{\eta}_o : \mathbf{A}) \cdot \boldsymbol{N}]\!] \cdot \boldsymbol{\delta}_s \cdot [\![\boldsymbol{P} \cdot \boldsymbol{N}]\!] \mathrm{d}A = 0 \end{aligned} \tag{36}$$

where $\boldsymbol{\delta}_s = \left[\left(\boldsymbol{\tau}_s^{(+)}\right)^{-1} + \left(\boldsymbol{\tau}_s^{(-)}\right)^{-1}\right]^{-1}$ is the additional stability tensor that arises due to the dependence of $\Delta\tilde{\boldsymbol{u}}$ on the traction jump $\llbracket \boldsymbol{P}\cdot\boldsymbol{N} \rrbracket$ through (30) and (34). The traction jump term along with the derived stability tensors distinguish the VMDG method from the popular Nitsche and interior penalty Galerkin methods. Similar to our previous work on VMDG [37, 39, 40], we neglect the traction jump term to simplify the formulation and reduce computational costs since the term is often relatively small [37, 40, 49]. The final form of the consistently derived and stabilized VMDG formulation for microscale deformation is then provided below as (37).

$$
\begin{aligned}
R\left(\boldsymbol{\eta}_o, \boldsymbol{\kappa}; \boldsymbol{\phi}, \boldsymbol{F}_{\mathrm{M}}\right) = {} & \underbrace{\int_{\Omega} \mathrm{GRAD}\, \boldsymbol{\eta}_o : \boldsymbol{P}\, \mathrm{d}V - \int_{\Gamma^+} \boldsymbol{\kappa} \llbracket \boldsymbol{X} \rrbracket \cdot \boldsymbol{P}_{\mathrm{M}} \boldsymbol{N}^{(+)} \mathrm{d}A}_{R0} \\
& + \underbrace{\int_{\Gamma^+} \left[\llbracket \boldsymbol{\eta}_o \rrbracket - \boldsymbol{\kappa} \llbracket \boldsymbol{X} \rrbracket\right] \cdot \boldsymbol{\tau}_s \cdot \left(\llbracket \boldsymbol{\phi} \rrbracket - \boldsymbol{F}_{\mathrm{M}} \llbracket \boldsymbol{X} \rrbracket\right) \mathrm{d}A}_{R1} \\
& - \underbrace{\int_{\Gamma^+} \left[\llbracket \boldsymbol{\eta}_o \rrbracket - \boldsymbol{\kappa} \llbracket \boldsymbol{X} \rrbracket\right] \cdot \left\{\boldsymbol{P} \cdot \boldsymbol{N}\right\} \mathrm{d}A}_{R2} \\
& - \underbrace{\int_{\Gamma^+} \left\{\left(\mathrm{GRAD}\, \boldsymbol{\eta}_o : \mathbf{A}\right) \cdot \boldsymbol{N}\right\} \cdot \left(\llbracket \boldsymbol{\phi} \rrbracket - \boldsymbol{F}_{\mathrm{M}} \llbracket \boldsymbol{X} \rrbracket\right) \mathrm{d}A}_{R3} = 0
\end{aligned}
\tag{37}
$$

For later elaborations on algorithmic modifications, we identify specific terms in the VMDG formulation. The volume integral in $R0$ weakly enforces equilibrium within the RVE while the surface integral imposes the macro-to-micro driving stress $\boldsymbol{P}_M$ and is the sole external driving force of the problem. The penalty term $R1$ stabilizes the VMDG formulation, and the consistent term $R2$ weakly enforces anti-periodicity of the tractions along Γ, thereby ensuring the VMDG method is variationally consistent. Besides ensuring that the VMDG method is symmetric, the symmetrizing term $R3$ also weakly imposes the periodicity of $\boldsymbol{\phi}$ along Γ.

The most significant contributions of the present paper that set it apart from our previous VMDG formulations are (a) the appearance of macroscopic or homogenized deformation gradient tensor $\boldsymbol{F}_{\mathrm{M}}$ in the penalty and symmetrizing terms, (b) the presence of weighting tensor $\boldsymbol{\kappa}$ in the penalty and consistent terms, and (c) the coupling of finite element surfaces along opposite boundaries separated by $[\![\boldsymbol{X}]\!]$ instead of across a closed interface. These tensors $\boldsymbol{F}_{\mathrm{M}}$ and $\boldsymbol{\kappa}$ constitute global variables that are collectively associated to boundary Γ as opposed to the local inelastic gap or damage variable $\boldsymbol{\zeta}$ defined pointwise along interfaces in [37-39]. These contributions collectively extend the VMDG framework to enable imposition of periodic boundary conditions on conforming and non-conforming meshes. Thus, the framework is now suited for micro-scale modeling of RVE with the goal of determining the overall effective properties of heterogeneous materials and alloys.

Remark:

Typically, stabilized methods require the calibration of stability parameters to ensure accuracy. While possibly requiring some effort, the use of carefully chosen constant parameters for each material region along the RVE boundary could still be appropriate for block shaped RVEs with periodic meshes. However, the use of spatially uniform parameters for microscale modeling of either non-periodic meshes or non-block RVEs could cause stability and accuracy issues since the interfacial physics between material regions on either side needs to be properly captured. The dependence of the stability tensor of the VMDG formulation on material properties of the two materials at the opposite boundaries naturally accommodates block RVE and self-periodic RVE modeling. Examples of spatial and temporal variations in VMDG stability tensors are given in [51].

3.3. Summary of consistent linearization and implementational aspects

The consistent linearization of the VMDG formulation in (37) is needed for the tangent stiffness matrix within the Newton-Raphson algorithm for solving the non-linear microscale behavior. We summarize the linearized form of the interface flux, jumps and material acoustic tensor in the Appendix. The reader is encouraged to refer to the Appendix and [40] for details regarding the linearization of the interface terms and [56] for the bulk terms. The contributions from the interface flux terms $K_{\boldsymbol{\eta}_o;\boldsymbol{\phi}}$ are then highlighted below in (38). The final linearized tangent stiffness components for the microscale behavior are presented in (39) - (42).

$$\begin{aligned} K_{\boldsymbol{\eta}_o;\boldsymbol{\phi}} = & \underbrace{\int_{\Omega} \mathrm{GRAD}\,\boldsymbol{\eta}_o : \mathbf{A} : \mathrm{GRAD}\,\Delta\boldsymbol{u}\,\mathrm{d}V}_{K0} + \underbrace{\int_{\Gamma^+} [\![\boldsymbol{\eta}_o]\!] \cdot \boldsymbol{\tau}_s \cdot [\![\Delta\boldsymbol{u}]\!]\,\mathrm{d}A}_{K1} \\ & \underbrace{-\int_{\Gamma^+} [\![\boldsymbol{\eta}_o]\!] \cdot \left\{ \left(\mathbf{A} : \mathrm{GRAD}\,\Delta\boldsymbol{u} \right) \cdot \boldsymbol{N} \right\} \mathrm{d}A}_{K2} \underbrace{- \int_{\Gamma^+} \left\{ \left(\mathrm{GRAD}\,\boldsymbol{\eta}_o : \mathbf{A} \right) \cdot \boldsymbol{N} \right\} \cdot [\![\Delta\boldsymbol{u}]\!]\,\mathrm{d}A}_{K3} \\ & \underbrace{-\int_{\Gamma^+} \left\{ \left(\mathrm{GRAD}\,\boldsymbol{\eta}_o : \boldsymbol{\Xi} : \mathrm{GRAD}\,\Delta\boldsymbol{u} \right) \cdot \boldsymbol{N} \right\} \cdot \left([\![\boldsymbol{\phi}]\!] - \boldsymbol{F}_{\mathrm{M}} [\![\boldsymbol{X}]\!] \right) \mathrm{d}A}_{K4} \end{aligned} \tag{38}$$

where the curvature tensor $\boldsymbol{\Xi}(\boldsymbol{F})$ is a sixth-order tensor of material moduli defined as in (39):

$$\boldsymbol{\Xi}(\boldsymbol{F}) = \frac{\partial^3 W}{\partial \boldsymbol{F}\,\partial \boldsymbol{F}\,\partial \boldsymbol{F}} \tag{39}$$

$$K_{\boldsymbol{\eta}_o;\boldsymbol{F}_{\mathrm{M}}} = \underbrace{-\int_{\Gamma^+} [\![\boldsymbol{\eta}_o]\!] \cdot \boldsymbol{\tau}_s \cdot \Delta\boldsymbol{\varepsilon}_{\mathrm{M}} [\![\boldsymbol{X}]\!]\,\mathrm{d}A}_{K1} + \underbrace{\int_{\Gamma^+} \left\{ \left(\mathrm{GRAD}\,\boldsymbol{\eta}_o : \mathbf{A} \right) \cdot \boldsymbol{N} \right\} \cdot \Delta\boldsymbol{\varepsilon}_{\mathrm{M}} [\![\boldsymbol{X}]\!]\,\mathrm{d}A}_{K3} \tag{40}$$

$$K_{\boldsymbol{\kappa};\boldsymbol{\phi}} = \underbrace{-\int_{\Gamma^+} \boldsymbol{\kappa} [\![\boldsymbol{X}]\!] \cdot \boldsymbol{\tau}_s \cdot [\![\Delta\boldsymbol{u}]\!]\,\mathrm{d}A}_{K1} + \underbrace{\int_{\Gamma^+} \boldsymbol{\kappa} [\![\boldsymbol{X}]\!] \cdot \left\{ \left(\mathbf{A} : \mathrm{GRAD}\,\Delta\boldsymbol{u} \right) \cdot \boldsymbol{N} \right\} \mathrm{d}A}_{K2} \tag{41}$$

$$K_{\boldsymbol{\kappa};\boldsymbol{F}_{\mathrm{M}}} = \underbrace{\int_{\Gamma^+} \boldsymbol{\kappa} [\![\boldsymbol{X}]\!] \cdot \boldsymbol{\tau}_s \cdot \Delta\boldsymbol{\varepsilon}_{\mathrm{M}} [\![\boldsymbol{X}]\!]\,\mathrm{d}A}_{K1} \tag{42}$$

In our previous studies [36, 39, 51], we have shown that the interface tangent stiffness $K_{\boldsymbol{\eta}_o;\boldsymbol{\phi}}$ is symmetric due to the existence of the interface potential functional for the VMDG method. It is obvious by inspection that the fourth tangent stiffness matrix in (42) is symmetric with respect to the variation $\boldsymbol{\kappa}$ and the incremental strain $\Delta\boldsymbol{\varepsilon}_M$. Notice that the third tangent stiffness matrix $K_{\boldsymbol{\kappa};\boldsymbol{\phi}}$ in (40) is the transpose of the second tangent stiffness matrix $K_{\boldsymbol{\eta}_o;\boldsymbol{F}_{\mathrm{M}}}$ in (41).

The implementation of the VMDG formulation into standard pure-displacement finite element (FE) codes requires two straightforward additions: (a) adding variables for $\boldsymbol{F}_{\mathrm{M}}$ and (b) computing force and stiffness terms along Γ^+. The macroscale tensor $\boldsymbol{F}_{\mathrm{M}}$ is straightforward to represent as $n_{\mathrm{sd}} \times n_{\mathrm{sd}}$ generalized degrees of freedom (DOFs) as proposed for example within [57]. A natural way to assign these DOFs into the FE code is to add n_{sd} so-called "macro" nodes into the model each having n_{sd} DOFs, and these nodes are appended to the connectivity of the "interface" elements mentioned in the next paragraph. The imposed components of the macroscale 1st Piola-Kirchhoff stress $\left\{\bar{P}_M\right\}_{j=1}^{n_P}$ are simply multiplied by the RVE volume V_0 and assigned as "nodal forces" to the macro-nodes. Constrained macroscale deformation gradient values $\left\{\bar{F}_M\right\}_{j=1}^{n_F}$ analogously give rise to nodal reactions $\left\{V_0 P_M\right\}_{j=1}^{n_F}$ that are obtained by the usual post-process method of FE displacement-based solutions. Also note that rigid body modes need to be suppressed in the discretization of the RVE microscale displacement field, e.g. by fixing node and partially constraining its neighbors.

Due to the element-local fine-scale representation, the smallest computational unit of the VMDG terms is an integral along a single boundary segment $\gamma_s \subset \Gamma^+$ such as in (31). The displacement and traction fields in these integrals require the nodes of the solid elements from sectors $\omega^{(+)}$ and $\omega^{(-)}$ adjacent to the segment and its image $\gamma^{(-)} = \wp\left(\gamma^{(+)}\right)$ as well as the macro nodes associated with $\boldsymbol{F}_{\mathrm{M}}$. For example, in the case of an RVE meshed with linear 4-node quadrilateral elements, all quantities for the surface integrals in (38) – (42) are computable in the discrete setting from the nodal displacements of two solid elements adjacent to γ_s and the macro nodes, implying a generalized "interface" element with (4+4+2)=10 nodes. The explicit form of the stiffness matrix for this VMDG interface element is given in equation (74) of the Appendix; note that one submatrix term turns out to be equivalent to previous forms of the VMDG stiffness matrix and thus analogous to symmetric interior penalty DG stiffness matrices. Also, small deformation counterparts (presented in Section 5) of these elements are implemented in MATLAB within the open-source interface mesh generation program DEIP [58], which has been extended to address periodic meshes in [43].

3.4. Macroscale material tangent modulus

While the emphasis on the computed results in Section 6 are on the microscale problem alone, the VMDG formulation is naturally suited for computing the macroscale material tangent moduli required for computational homogenization methods. Due to the location of the macroscale stress $\boldsymbol{P}_{\mathrm{M}}$ in the residual form (37), the computation of the total derivative $d\boldsymbol{P}_{\mathrm{M}} / d\boldsymbol{F}_{\mathrm{M}}$ follows from the linearized terms given in Section 3.3 and the Appendix after a short algebraic manipulation, along the lines of [10, 16]. Let $\bar{\mathbf{K}}_{\boldsymbol{\eta}_o;\boldsymbol{\phi}}$, $\bar{\mathbf{K}}_{\boldsymbol{\eta}_o;\boldsymbol{F}_{\mathrm{M}}}$, $\bar{\mathbf{K}}_{\boldsymbol{\kappa};\boldsymbol{\phi}}$, and $\bar{\mathbf{K}}_{\boldsymbol{\kappa};\boldsymbol{F}_{\mathrm{M}}}$ denote the global assembled stiffness matrices from the RVE interior and boundary given in the Appendix, with rigid translation suppressed in $\bar{\mathbf{K}}_{\boldsymbol{\eta}_o;\boldsymbol{\phi}}$. Then the macroscale material tangent components follow as:

$$dP_{\mathrm{M},ij} / dF_{\mathrm{M},kl} = \frac{1}{V_0}\left[\bar{\mathbf{K}}_{\boldsymbol{\kappa};\boldsymbol{F}_{\mathrm{M}}}\right]_{ijkl} - \frac{1}{V_0}\left[\bar{\mathbf{K}}_{\boldsymbol{\kappa};\boldsymbol{\phi}}\left(\bar{\mathbf{K}}_{\boldsymbol{\eta}_o;\boldsymbol{\phi}}\right)^{-1}\bar{\mathbf{K}}_{\boldsymbol{\eta}_o;\boldsymbol{F}_{\mathrm{M}}}\right]_{ijkl} \tag{43}$$

We emphasize that these matrices are identical to those needed by the Newton-Raphson algorithm with zero modification or manipulation, making this calculation easy to implement.

4. Algorithmic modifications to VMDG method

The attractive features of the proposed VMDG formulation for microscale modeling lie with the consistently derived expressions for the stability tensors and numerical fluxes, which account for material and geometric nonlinearity. The complexity and implementational cost of the method can be reduced by adjusting the residual force vector and tangent matrix, with possible consequences to the stability, accuracy and consistency of the method. These simplifications are summarized in Table 1 and range from removing the curvature tensor $\boldsymbol{\Xi}$, to removing the symmetric term, to freezing the acoustic tensor during iterations. However, these modifications could affect the variational, adjoint or/and algorithmic consistencies of the method. The reader is referred to [51] for the definition of the three types of consistency as well as other comments. In particular, loss of adjoint consistency can reduce the convergence rate of the L_2 displacement error norm with respect to mesh refinement, and loss of algorithmic consistency may reduce the convergence rate of the iterated residual within the Newton-Raphson method. These modifications are assessed numerically in Section 6.

Table 1. Summary of the residual and tangent stiffness terms

	Method	Residual	Tangent matrices			
			$K_{\eta_o;\phi}$	$K_{\eta_o;\bar{F}}$	Algo. cons.	Tang. Symm.
1	VMDG	$R1, R2, R3$	$K1, K2, K3, K4$	$K1, K3$	Y	Y
2	VMDGs	$R1, R2, R3$	$K1, K2, K3$	$K1, K3$	N	Y
3	IVMDG	$R1, R2$	$K1, K2$	$K1$	Y	N
4	IVMDGs	$R1, R2$	$K1, K2, K3$	$K1, K3$	N	Y
5	RVMDG	$R1, R2, \bar{R}_o3$	$K1, K2, \bar{K}_o3$	$K1, \bar{K}_o3$	Y	N
6	RVMDGs	$R1, R2, \bar{R}_o3$	$K1, K2, K3$	$K1, K3$	N	Y

4.1. VMDGs method

The derivation of the closed form of the curvature tensor $\boldsymbol{\Xi}$, a sixth order tensor, can be very involved especially for complex material models. For example, the case of Von Mises plasticity requires more than the second variational derivative of radial return algorithm and the accompanying nonlinear kinematic tensors [50]. However, the contribution of the $K4$ term containing $\boldsymbol{\Xi}$ can be very small when the discretized deformation jump $[\![\boldsymbol{\phi}]\!]$ is close to zero. Therefore we define the VMDGs method by removing the $K4$ term from the tangent stiffness matrix while still retaining the VMDG residual force vector, where “s” refers to shortening or symmetrizing. Row 2 of Table 1 shows that VMDGs retains all the terms in VMDG except the reduction of $K_{\boldsymbol{\eta}_o;\boldsymbol{\phi}}$ to the form expressed in (44). While this new formulation does not possess algorithmic consistentency, it is variationally consistent, adjoint consistent, and symmetric. Hence, the VMDGs is simple to implement and provide computational cost savings.

$$\begin{aligned} K_{\boldsymbol{\eta}_o;\boldsymbol{\phi}} = K\left(\boldsymbol{\eta}_o, \Delta\boldsymbol{u}; \boldsymbol{\phi}\right) = & \underbrace{\int_{\Omega} \mathrm{GRAD}\,\boldsymbol{\eta}_o : \mathbf{A} : \mathrm{GRAD}\;\Delta\boldsymbol{u}\;\mathrm{d}V}_{K0} + \underbrace{\int_{\Gamma^+} \llbracket \boldsymbol{\eta}_o \rrbracket \cdot \boldsymbol{\tau}_s \cdot \llbracket \Delta\boldsymbol{u} \rrbracket\,\mathrm{d}A}_{K1} \\ & - \underbrace{\int_{\Gamma^+} \llbracket \boldsymbol{\eta}_o \rrbracket \cdot \left\{\left(\mathbf{A} : \mathrm{GRAD}\;\Delta\boldsymbol{u}\right) \cdot \boldsymbol{N}\right\}\,\mathrm{d}A}_{K2} - \underbrace{\int_{\Gamma^+} \left\{\left(\mathrm{GRAD}\;\boldsymbol{\eta}_o : \mathbf{A}\right) \cdot \boldsymbol{N}\right\} \cdot \llbracket \Delta\boldsymbol{u} \rrbracket\,\mathrm{d}A}_{K3} \end{aligned} \tag{44}$$

4.2. IVMDG/ IVMDGs method: incomplete interior penalty method

The IVMDG method is a further modification of VMDG formulation where the symmetrizing term is removed from the residual force vector and the tangent stiffness matrix, analogous to the “Incomplete” interior penalty method. Hence, the method inherits the algorithmic consistency properties but is non-symmetric. The third row of Table 1 highlights the terms present in the residual vector and tangent matrix. For completeness, the reduced residual and linearized weak form are expressed in (45) – (47).

$$\begin{aligned} R\left(\boldsymbol{\eta}_o, \boldsymbol{\kappa}; \boldsymbol{\phi}, \boldsymbol{F}_{\mathrm{M}}\right) = & \underbrace{\int_{\Omega} \mathrm{GRAD}\;\boldsymbol{\eta}_o : \boldsymbol{P}\,\mathrm{d}V - \int_{\Gamma^+} \boldsymbol{\kappa} \llbracket \boldsymbol{X} \rrbracket \cdot \boldsymbol{P}_{\mathrm{M}} \boldsymbol{N}^{(+)}\mathrm{d}A}_{R0} \\ & + \underbrace{\int_{\Gamma^+} \left[\llbracket \boldsymbol{\eta}_o \rrbracket - \boldsymbol{\kappa} \llbracket \boldsymbol{X} \rrbracket\right] \cdot \boldsymbol{\tau}_s \cdot \left(\llbracket \boldsymbol{\phi} \rrbracket - \boldsymbol{F}_{\mathrm{M}} \llbracket \boldsymbol{X} \rrbracket\right)\mathrm{d}A}_{R1} \\ & - \underbrace{\int_{\Gamma^+} \left[\llbracket \boldsymbol{\eta}_o \rrbracket - \boldsymbol{\kappa} \llbracket \boldsymbol{X} \rrbracket\right] \cdot \left\{\boldsymbol{P} \cdot \boldsymbol{N}\right\}\,\mathrm{d}A}_{R2} = 0 \end{aligned} \tag{45}$$

$$\begin{aligned} K_{\boldsymbol{\eta}_o;\boldsymbol{\phi}} = K\left(\boldsymbol{\eta}_o, \Delta\boldsymbol{u}; \boldsymbol{\phi}\right) = & \underbrace{\int_{\Omega} \mathrm{GRAD}\,\boldsymbol{\eta}_o : \mathbf{A} : \mathrm{GRAD}\;\Delta\boldsymbol{u}\;\mathrm{d}V}_{K0} + \underbrace{\int_{\Gamma^+} \llbracket \boldsymbol{\eta}_o \rrbracket \cdot \boldsymbol{\tau}_s \cdot \llbracket \Delta\boldsymbol{u} \rrbracket\,\mathrm{d}A}_{K1} \\ & - \underbrace{\int_{\Gamma^+} \llbracket \boldsymbol{\eta}_o \rrbracket \cdot \left\{\left(\mathbf{A} : \mathrm{GRAD}\;\Delta\boldsymbol{u}\right) \cdot \boldsymbol{N}\right\}\,\mathrm{d}A}_{K2} \end{aligned} \tag{46}$$

$$K_{\boldsymbol{\eta}_o;\boldsymbol{F}_\mathrm{M}} = K\left(\boldsymbol{\eta}_o, \Delta\boldsymbol{\varepsilon}_\mathrm{M}; \boldsymbol{F}_\mathrm{M}\right) = \underbrace{-\int_{\Gamma^+} [\![\boldsymbol{\eta}_o]\!] \cdot \boldsymbol{\tau}_s \cdot [\![\Delta\boldsymbol{\varepsilon}_\mathrm{M}]\!] \,\mathrm{d}A}_{K1} \tag{47}$$

While this method is the simplest that retains variational consistency, the loss of adjoint consistency leads to some drawbacks, including possible reduced accuracy, reduced convergence rate of displacement error, and extra data requirements for non-symmetric solvers. To combat the latter similar to [51], the IVMDGs is proposed by restoring the symmetry according to the fourth row of Table 1, namely using the tangent of the VMDGs method. Therefore, this method lacks both adjoint consistency and algorithmic consistency, and this trade-off may impact its numerical performance.

4.3. RVMDG/ RVMDGs method: reference configuration acoustic tensor $\mathbf{A}_o$

The RVMDG method is designed as a compromise between the original VMDG and IVMDG methods by freezing the deformation gradient $\boldsymbol{F} = \mathbf{1}$ to the reference configuration (denoted by "R") and consequently freezing the acoustic tensor $\mathbf{A} = \mathbf{A}_o$ in the symmetrizing term. The residual force and tangent matrix in the fifth row of the Table 1 are then defined in terms of $\bar{R}_o 3$ and $\bar{K}_o 3$. For completeness, the reduced residual force vector and linearized weak form are expressed in (48) – (50).

$$\begin{aligned} R\left(\boldsymbol{\eta}_o, \boldsymbol{\kappa}; \boldsymbol{\phi}, \boldsymbol{F}_\mathrm{M}\right) = & \underbrace{\int_\Omega \mathrm{GRAD}\,\boldsymbol{\eta}_o : \boldsymbol{P} \,\mathrm{d}V - \int_{\Gamma^+} \boldsymbol{\kappa} [\![\boldsymbol{X}]\!] \cdot \boldsymbol{P}_\mathrm{M} \boldsymbol{N}^{(+)} \mathrm{d}A}_{R0} \\ & \underbrace{+\int_{\Gamma^+} \left[[\![\boldsymbol{\eta}_o]\!] - \boldsymbol{\kappa}[\![\boldsymbol{X}]\!]\right] \cdot \boldsymbol{\tau}_s \cdot \left([\![\boldsymbol{\phi}]\!] - \boldsymbol{F}_\mathrm{M}[\![\boldsymbol{X}]\!]\right) \mathrm{d}A}_{R1} \\ & \underbrace{-\int_{\Gamma^+} \left[[\![\boldsymbol{\eta}_o]\!] - \boldsymbol{\kappa}[\![\boldsymbol{X}]\!]\right] \cdot \left\{\boldsymbol{P} \cdot \boldsymbol{N}\right\} \mathrm{d}A}_{R2} \\ & \underbrace{-\int_{\Gamma^+} \left\{\left(\mathrm{GRAD}\,\boldsymbol{\eta}_o : \mathbf{A}_o\right) \cdot \boldsymbol{N}\right\} \cdot \left([\![\boldsymbol{\phi}]\!] - \boldsymbol{F}_\mathrm{M}[\![\boldsymbol{X}]\!]\right) \mathrm{d}A}_{\bar{R}_o 3} = 0 \end{aligned} \tag{48}$$

$$\begin{aligned} K_{\boldsymbol{\eta}_o;\boldsymbol{\phi}} = {} & \underbrace{\int_{\Omega} \mathrm{GRAD}\,\boldsymbol{\eta}_o : \mathbf{A} : \mathrm{GRAD}\,\Delta\boldsymbol{u}\,\mathrm{d}V}_{K0} + \underbrace{\int_{\Gamma^+} [\![\boldsymbol{\eta}_o]\!] \cdot \boldsymbol{\tau}_s \cdot [\![\Delta\boldsymbol{u}]\!]\,\mathrm{d}A}_{K1} \\ & \underbrace{- \int_{\Gamma^+} [\![\boldsymbol{\eta}_o]\!] \cdot \left\{ \left(\mathbf{A} : \mathrm{GRAD}\,\Delta\boldsymbol{u} \right) \cdot \boldsymbol{N} \right\} \mathrm{d}A}_{K2} \underbrace{- \int_{\Gamma^+} \left\{ \left(\mathrm{GRAD}\,\boldsymbol{\eta}_o : \mathbf{A}_o \right) \cdot \boldsymbol{N} \right\} \cdot [\![\Delta\boldsymbol{u}]\!]\,\mathrm{d}A}_{\bar{K}_o 3} \end{aligned} \tag{49}$$

$$K_{\boldsymbol{\eta}_o;\boldsymbol{F}_{\mathrm{M}}} = \underbrace{- \int_{\Gamma^+} [\![\boldsymbol{\eta}_o]\!] \cdot \boldsymbol{\tau}_s \cdot [\![\Delta\boldsymbol{\varepsilon}_{\mathrm{M}}]\!]\,\mathrm{d}A}_{K1} + \underbrace{\int_{\Gamma^+} \left\{ \left(\mathrm{GRAD}\,\boldsymbol{\eta}_o : \mathbf{A}_o \right) \cdot \boldsymbol{N} \right\} \cdot \Delta\boldsymbol{\varepsilon}_{\mathrm{M}}\,\mathrm{d}A}_{\bar{K}_o 3} \tag{50}$$

While the RVMDG residual has the same structure as VMDG, the linearized weak form does not contain the curvature tensor due to the fixed acoustic tensor in the symmetric term. Note that RVMDG has a non-symmetric tangent stiffness similar to IVMDG and has a number of terms similar to VMDGs. Like IVMDGs, the RVMDGs method is developed by sacrificing the algorithmic consistency of the RVMDG method to recover tangent symmetry by substituting $\bar{K}_o 3$ for $K3$; see the sixth row of Table 1. We remark that since $K3$ is the transpose of $K2$, RVMDGs is less expensive in comparison with RVMDG.

5. Specialization of the VMDG formulation to small strains

The VMDG method can be specialized to enforce PBC on RVE undergoing small displacements and strains; the small strain kinematics formulation is presented for completeness. When the deformation is small, the second order terms in the Green-Lagrange strain are negligible, and the displacement gradient evaluated in the undeformed configuration can be approximated with that evaluated in the current configuration. Hence, the VMDG method can be formulated based on the current configuration $\boldsymbol{x} = \boldsymbol{\phi}(\boldsymbol{X}, t)$. The microscopic displacement $\boldsymbol{u}$ is split into the linear displacement $\boldsymbol{\varepsilon}_{\mathrm{M}}\,\boldsymbol{x}$ from the macroscale and the displacement fluctuation $\tilde{\boldsymbol{u}}$ according to (51), where the fluctuations at each pair $\left\{ \boldsymbol{x}^{(+)}, \boldsymbol{x}^{(-)} \right\}$ are set equal to enforce the periodicity condition. The displacement jump at the RVE boundaries can then be expressed as (52).

$$\boldsymbol{u}^{(\alpha)}\left(\boldsymbol{x}^{(\alpha)}\right) = \boldsymbol{\varepsilon}_{\mathrm{M}}\,\boldsymbol{x}^{(\alpha)} + \tilde{\boldsymbol{u}}^{(\alpha)}, \qquad \tilde{\boldsymbol{u}}^{(+)}\left(\boldsymbol{x}^{(+)}\right) = \tilde{\boldsymbol{u}}^{(-)}\left(\boldsymbol{x}^{(-)}\right) \tag{51}$$

$$\boldsymbol{u}^{(+)} - \boldsymbol{u}^{(-)} = \boldsymbol{\varepsilon}_M \llbracket \boldsymbol{x} \rrbracket \tag{52}$$

The associated strong form and weak form of the mixed RVE problem at small strains is then posed in terms of the displacement and Lagrange multiplier fields. The ensuing steps of variational multiscale modeling are then followed with analogy to the large strain context, where the fine-scale problem is already linear and thus simpler. The resulting small strain VMDG formulation emerges as: Find $\{\boldsymbol{u}, \boldsymbol{\varepsilon}_{\mathrm{M}}\} \in \mathcal{S} \times \mathcal{T}_F$ such that for all $\{\boldsymbol{w}, \boldsymbol{\kappa}\} \in \mathcal{S} \times \mathcal{T}_0$:

$$\begin{aligned} &\underbrace{\int_\Omega \boldsymbol{\varepsilon}(\boldsymbol{w}) : \mathbf{C} : \boldsymbol{\varepsilon}(\boldsymbol{u}) \, \mathrm{d}V - V_0 \boldsymbol{\kappa} : \boldsymbol{\sigma}_M}_{R0} + \underbrace{\int_{\Gamma^+} \left(\llbracket \boldsymbol{w} \rrbracket - \boldsymbol{\kappa} \llbracket \boldsymbol{x} \rrbracket \right) \cdot \boldsymbol{\tau}_s \cdot \left(\llbracket \boldsymbol{u} \rrbracket - \boldsymbol{\varepsilon}_{\mathrm{M}} \llbracket \boldsymbol{x} \rrbracket \right) \mathrm{d}\Gamma}_{R1} \\ &- \underbrace{\int_{\Gamma^+} \left(\llbracket \boldsymbol{w} \rrbracket - \boldsymbol{\kappa} \llbracket \boldsymbol{x} \rrbracket \right) \cdot \left\{ \mathbf{C} : \boldsymbol{\varepsilon}(\boldsymbol{u}) \cdot \boldsymbol{n} \right\} \mathrm{d}\Gamma}_{R2} - \underbrace{\int_{\Gamma^+} \left\{ \mathbf{C} : \boldsymbol{\varepsilon}(\boldsymbol{w}) \cdot \boldsymbol{n} \right\} \cdot \left(\llbracket \boldsymbol{u} \rrbracket - \boldsymbol{\varepsilon}_{\mathrm{M}} \llbracket \boldsymbol{x} \rrbracket \right) \mathrm{d}\Gamma}_{R3} = 0 \end{aligned} \tag{53}$$

where $\boldsymbol{w}$ is the weighting function, $\boldsymbol{\varepsilon}$ is the symmetric gradient operator, and the moduli tensor $\mathbf{C}$ is obtained from the Cauchy stress $\boldsymbol{\sigma}$ operator $\boldsymbol{\sigma}(\boldsymbol{u}) = \mathbf{C} : \boldsymbol{\varepsilon}(\boldsymbol{u})$. The deformation of the microscale domain is driven by the macroscale Cauchy stress $\boldsymbol{\sigma}_{\mathrm{M}}$ and engineering strain $\boldsymbol{\varepsilon}_{\mathrm{M}}$; as before, only one component of stress or strain is imposed at a time. The appearance of the formulation in the small strain context (53) resembles the large strain counterpart in (37). The bulk term $R0$, the penalty term $R1$, the consistency term $R2$, and the symmetric term $R3$ are present. However, the sixth-order curvature tensor does not appear in the stiffness matrix since the problem is linear. Hence, the implementation is simpler and straightforward. In the numerical section, we will argue that the VMDG method is very robust and stable for RVE undergoing both finite and small strains.

6. Numerical Results

In this section, we investigate the performance of the proposed interface formulation across a range of 2-dimensional and 3-dimensional RVE domains subjected to small and large strains. The following compressible Neo Hookean material model is employed for modeling large strain, and plane strain conditions are assumed in all 2-dimensional cases:

$$\psi(\boldsymbol{F}) = \frac{1}{2}\lambda(\det\boldsymbol{F} - 1)^2 - \mu\ln(\det\boldsymbol{F}) + \frac{1}{2}\mu\left(\text{tr}\,\left(\boldsymbol{F}^T\boldsymbol{F}\right) - 3\right) \tag{54}$$

$$\boldsymbol{P} = \lambda\det\boldsymbol{F}(\det\boldsymbol{F} - 1)\boldsymbol{F}^{-T} + \mu\left(\boldsymbol{F}^{-T} + \boldsymbol{F}\right) \tag{55}$$

The bubble functions $b_s^{(\alpha)}$ used for evaluating the stability tensors $\boldsymbol{\tau}_s^{(\alpha)}$ for 2-dimensional and 3-dimensional (2-D and 3-D) element types are listed in [51], and all calculations are done using full numerical quadrature. The first example highlights the stress driven capability of the method while the other examples are strain driven problems. In the first numerical example, a patch test using a composite rectangular block is implemented in the small strain context to check the variational consistency and accuracy of the FE solutions produced from enforcing PBC on RVE using the VMDG method. Convergence rates of displacement error in the L_2 norm and H^1 semi-norm are performed for different element types.

The accuracy and variational consistency of the VMDG method for enforcing PBC on periodic and non-periodic RVE are evaluated in the second example in comparison with the mortar method. Reference solutions are taken from highly refined meshes, which is justified when a formulation does not exhibit stability issues. This is followed by another numerical example where a 2-D RVE consisting of periodic microstructures is subjected to an average tensile strain. The model example is designed as a polycrystalline sample of a metallic alloy to serve as a practical application with interest to the broader research community. The effectiveness of the standard VMDG method is first studied for representing the material response and required periodicity of the solution fields across RVE domain before exploring the robustness, accuracy and computation cost associated with other methods belonging to the VMDG algorithmic family.

Finally, the accuracy and robustness of the VMDG method to weakly enforce PBC on complex truly periodic 3-D microstructures are studied. Initially, isotropic material behavior is employed in a patch test to compare with the LM method. Then, the anisotropic properties of a single phase

$\alpha-$Ti-6Al alloy are assigned in a periodic RVE consisting of a 100-grain microstructure. Instances of random and fiber textures are modeled to assess the VMDG method's performance for polycrystalline materials.

Remark:

The following numerical problems all employ hyperelastic materials such that the VMDG method has an underlying potential energy form. Allowing for inelastic material response requires that the material history is also tracked at the quadrature points along the boundary segments due to the appearance of the stress tensor in the flux terms. Additionally, the derived fine-scale stability terms should account for the material history dependence. Such aspects were addressed for the VMDG method [50] in the context of small deformation isotropic plasticity. A forthcoming work will establish the algorithmic performance of the VMDG method for anisotropic crystal plasticity with interfacial debonding.

6.1. Rectangular composite block

Herein, we evaluate the variational consistency of the VMDG method by performing a convergence rate study using different element types. The coarsest meshes are shown in Figure 5, and the refined meshes are obtained using uniform bisection. The details of the mesh hierarchy are presented in Table 2. We model a macro-stress driven RVE problem where an average shear stress $\bar{\sigma}_{\mathrm{M,xy}} = 10\ \mathrm{MPa}$ and zero axial stresses are prescribed on a 4 mm × 4 mm rectangular composite domain consisting of two materials. The elastic moduli of the central rectangular domain and outer domain are $\mathrm{E}^1 = 500\,\mathrm{MPa}$ and $\mathrm{E}^2 = 100\,\mathrm{MPa}$, respectively, while the Poisson ratios are the same with $\upsilon^1 = \upsilon^2 = 0.25$. Figure 6 shows the average strain γ_{M} response plotted against the characteristic mesh parameter h. For all element types considered, the predicted average strains approach the reference value as the mesh is refined, where the reference is obtained on a further refined grid. The percent errors in the average strain from the coarsest approximation are

0.93%, 0.55%, 0.12% and 0.06% for T3, Q4, T6 and Q9 elements respectively. This trend is consistent with the behavior of other stabilized methods such as in [48].

The reference error $\boldsymbol{e} = \boldsymbol{u}^f - \boldsymbol{u}^h$ between the computed $\boldsymbol{u}^h$ and highly refined $\boldsymbol{u}^f$ solutions are evaluated in the L_2 norm and H^1 semi norm using (56) and (57) to estimate the global measure of accuracy of the numerical results.

$$\|\boldsymbol{v}\|_{L_2(w)} = \sqrt{\int_w \boldsymbol{v} \cdot \boldsymbol{v} \, \mathrm{d}\Omega} \tag{56}$$

$$\|\boldsymbol{v}\|_{H^1(w)} = \sqrt{\int_w \nabla \boldsymbol{v} : \nabla \boldsymbol{v} \, \mathrm{d}\Omega} \tag{57}$$

The results presented in Figure 7 show that the convergence rates of the linear elements are consistent with finite element definition of the rate of convergence of a primal field. These values which are approximately 2 and 1 correspond to $k+1$ and k for L_2 norm and H^1 semi norm, where k is the highest degree of the polynomial basis functions. However, the rates of the convergence of the quadratic elements are affected by the low regularity of the displacement field solution attributed to the sharp corners of the inner domain. Nonetheless, the average strain as well as the microscale displacement field from all element types converges as the element size is reduced.

Table 2. Listing of elements and nodes in the mesh hierarchy

Mesh name	Q4		Q9		T3		T6	
	Elements	Nodes	Elements	Nodes	Elements	Nodes	Elements	Nodes
Coarse	64	81	64	289	128	81	128	289
Medium	256	289	256	1089	512	289	512	1089
Fine	1024	1089	1024	4225	2048	1089	2048	4225
Very fine	4096	4225	4096	16641	8192	4225	8192	16641

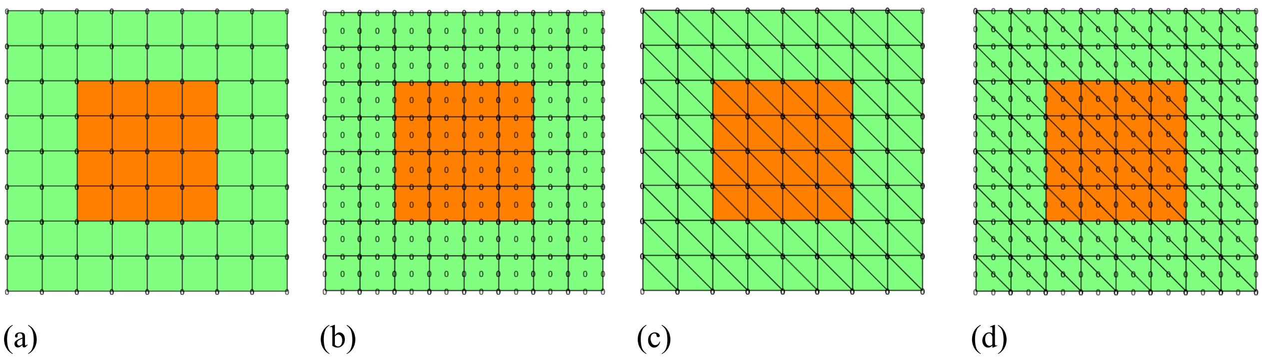

Figure 5. Mesh hierarchy: (a) 64 elements Q4; (b) 64 elements Q9; (c) 128 elements T3; (d) 128 elements T6

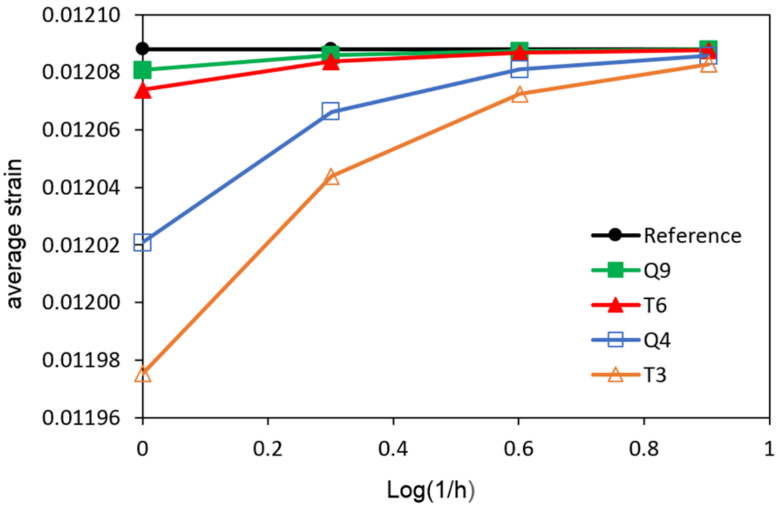

Figure 6. Convergence of average strain γ_{M} for different element types

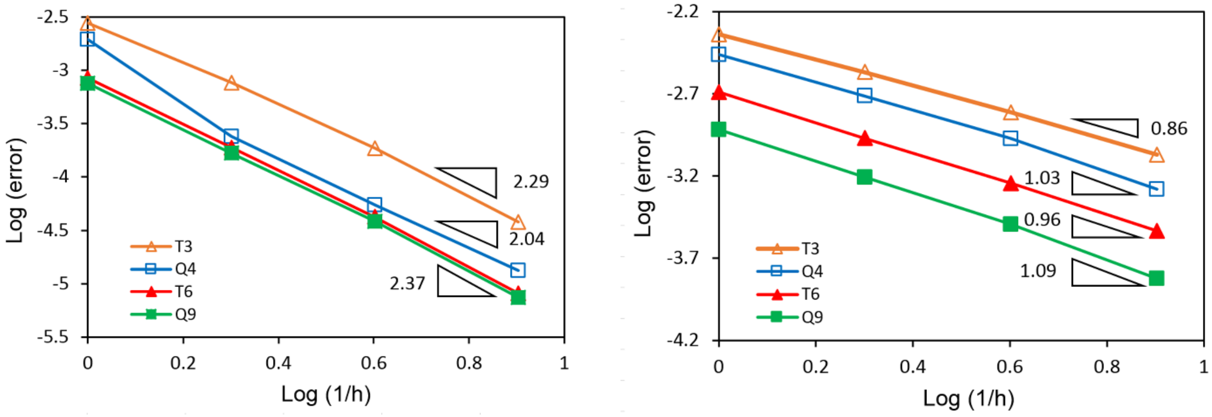

(a) (b)

Figure 7. Convergence rates of the error: (a) L_2 norm of displacement; (b) H^1 semi norm of displacement

For a visual comparison, a domain consisting of uniform material properties $\mathrm{E} = 100\,\mathrm{MPa}$, $\upsilon = 0.25$ is simulated, and the contour plot of displacement u_x is presented in Figure 8 (a), where the deformed shape has been exaggerated by a factor of 10. The maximum displacement of $0.0625\,\mathrm{mm}$ is produced at the top edge, and uniform gradient fields $\gamma_{xy} = 0.0156$ and $\sigma_{xy} = 10$ MPa are reproduced. The displacement u_x contour plot of the composite block RVE is shown in Figure 8 (b), where maximum displacement equals $0.0481\mathrm{mm}$. The reduced displacement and warping deformed shape of the composite block are attributed to the presence of a stiffer material at the center.

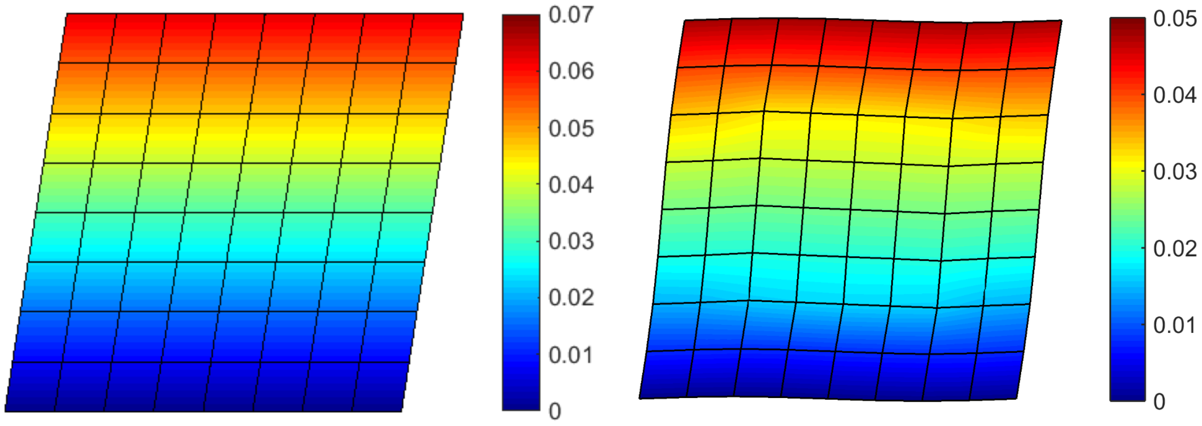

(a) (b)

Figure 8. Displacement u_x (mm) on deformed configuration $\times 10$: (a) homogenous block; (b) composite block

6.2. Periodic and Non-Periodic RVE mesh with circular voids

The efficiency of the proposed method for enforcing PBC on periodic and non-periodic meshes is evaluated herein. A $2\,\text{mm} \times 2\,\text{mm}$ RVE with four circular voids, each having a radius of $0.2\,\text{mm}$ and centered within $1\,\text{mm} \times 1\,\text{mm}$ squares, is subjected to a small deformation gradient $\bar{\boldsymbol{F}}_{\text{M}}$ with shearing components according to (58) applied in twenty equal load steps. The material properties are specified as $\text{E} = 70\,\text{GPa}$ and $\upsilon = 0.3$. The discretized RVE containing a periodic mesh of 1600 linear quadrilateral elements is shown in Figure 9(a), and its non-periodic counterparts containing 1880 linear quadrilateral elements are shown in Figure 9(b) – (c). The non-periodic mesh A is a mirror image of the non-periodic mesh B. The RVEs with the same material definition and mesh resolution described herein have been modeled earlier in [18] using the mortar method. The P_{12} component of the first PK stress tensor obtained from the RVE modeling using the proposed VMDG method are compared with those from the mortar method in [18]. For a highly refined mesh, P_{12} produced from the VMDG method is equal to $3582.3\,\text{MPa}$ for both the periodic mesh and non-periodic mesh. This value is used as the reference value to compute percentage error instead of using P_{12} from coarser periodic mesh in [18]. The results presented in Figure 10 show that the first PK stress tensor produced from the VMDG method are $3636.41\,\text{MPa}$, 3633.53 MPa and 3633.54 MPa for the periodic mesh, non-periodic mesh A and non-periodic mesh B while the equivalent stresses produced by mortar method are recorded from [18] as $3658.73\,\text{MPa}$, 3654.43 MPa and 3653.75 MPa. The VMDG solutions have a percentage error of 1.51%, 1.43% and 1.43% while the mortar method solutions have a percentage error of 2.13%, 2.01% and 1.99% for periodic, non-periodic A and non-periodic B meshes. The VMDG solutions are very close to the solutions from mortar method, and the VMDG method produced quite similar stress results for both non-periodic mesh A and non-periodic mesh B. Note that exact form of the neo-Hookean material model is not recorded in [18], which precludes making an exact comparison.

$$\bar{\boldsymbol{F}}_{\mathrm{M}} = \begin{bmatrix} 1.0 & 0.1 \\ 0.1 & 1.0 \end{bmatrix} \tag{58}$$

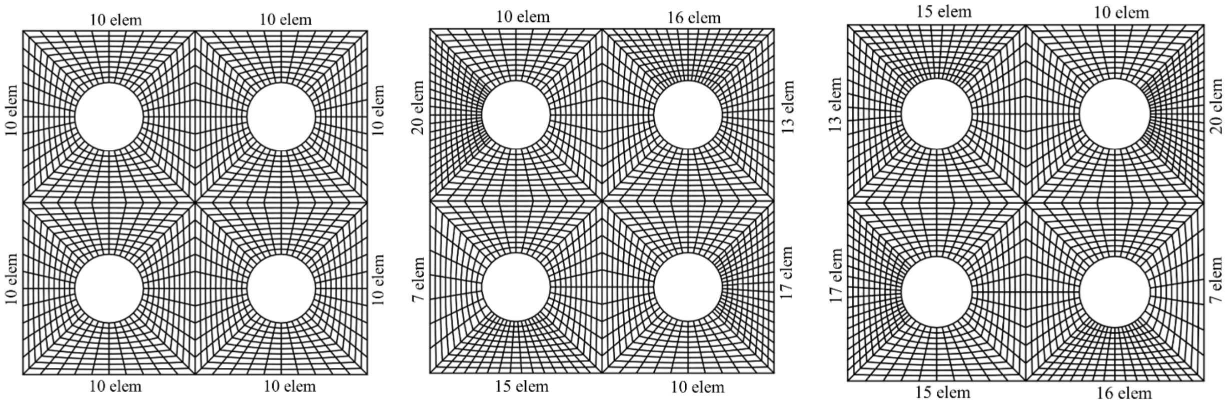

(a) (b) (c)

Figure 9. Finite element RVE with (a) periodic mesh:1600 linear quadratic elements; (b) Non-periodic mesh A: 1880 elements; (c) Non-periodic mesh B: 1880 elements

To briefly report the methods' algorithmic efficiency, the iterated residual norms from the Newton solver during one of the twenty equally spaced load increments are tabulated in Table 3. The results show that the VMDG method is fully linearized and algorithmically converged faster than the mortar method.

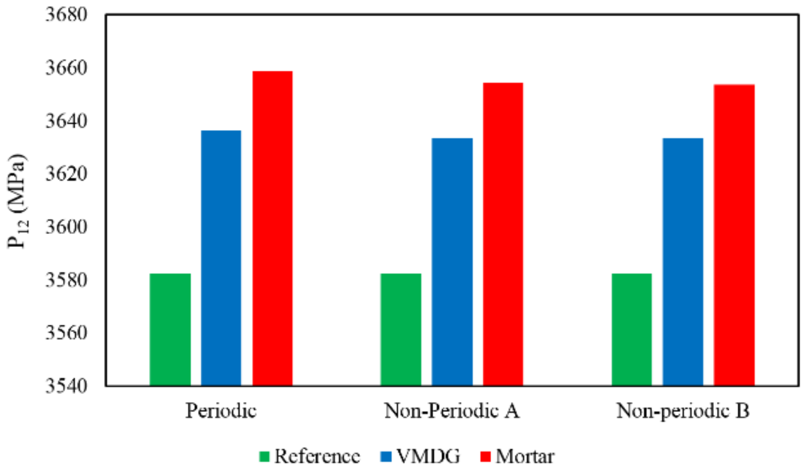

Figure 10. Comparison of first Piola-Kirchhoff stress from each method versus refined solution

Table 3. Evolution of the residual L_2 norm for each method

Iteration number	Mortar Method [18]	VMDG
1	8.47687	0.288937×10^{-4}
2	0.203536	0.812551×10^{-9}
3	0.134021×10^{-4}	0.311889×10^{-15}
4	0.358867×10^{-11}	-

Next, we further analyze the features of the VMDG computed response on the periodic and non-periodic meshes. The shear stress σ_{12} contour plot of the results from the VMDG formulation are presented in Figure 11. There is no appreciable difference in the contour plots from all meshes considered except nearby the voids. A similar value of local maximum shear stress of 1734 MPa is produced by both the periodic and non-periodic meshes. Additionally, refinement by mesh subdivision was carried out, and the macroscale stress $P_{\mathrm{M},12}$ for each mesh is recorded in Figure

12. The periodic mesh and the non-periodic mesh results clearly converge towards each other with reduced element size h. Also, the computed stress slightly decreases with refinement, which is logical since the macroscale strain is prescribed and the FE approximation generally becomes less stiff with refinement.

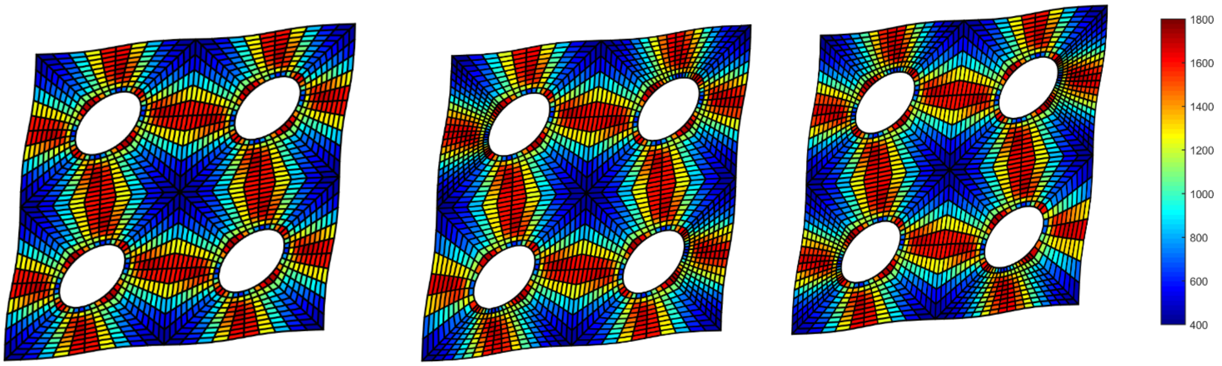

(a) (b) (c)

Figure 11. The Cauchy shear stress σ_{12} contour plot: (a) periodic mesh (b) non-periodic mesh A (c) non-periodic mesh B

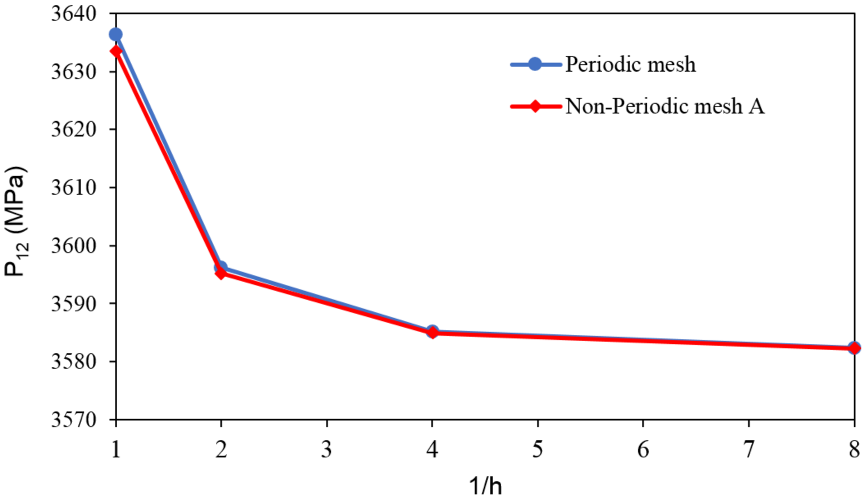

Figure 12. Convergence of macroscale stress for periodic and non-periodic meshes

6.3. 2-D microstructure containing 6 grains

The trade-offs in efficiency and accuracy of the VMDG family of methods is studied herein for enforcing PBC on a polycrystalline microstructure. The 6-grain periodic RVE is generated in 2 steps: (1) a standard non-periodic microstructure is generated using an open-source program, and (2) adjustments are made to selected nodes and regions along the domain edges. First, a 1 mm × 1 mm two-dimensional RVE non-periodic microstructure containing 10 grains is generated using Neper open source software package [59] as shown in Figure 13 (a). The reader is encouraged to consult its user manual for details on the commands for tessellating and meshing the standard 10 grain microstructure.

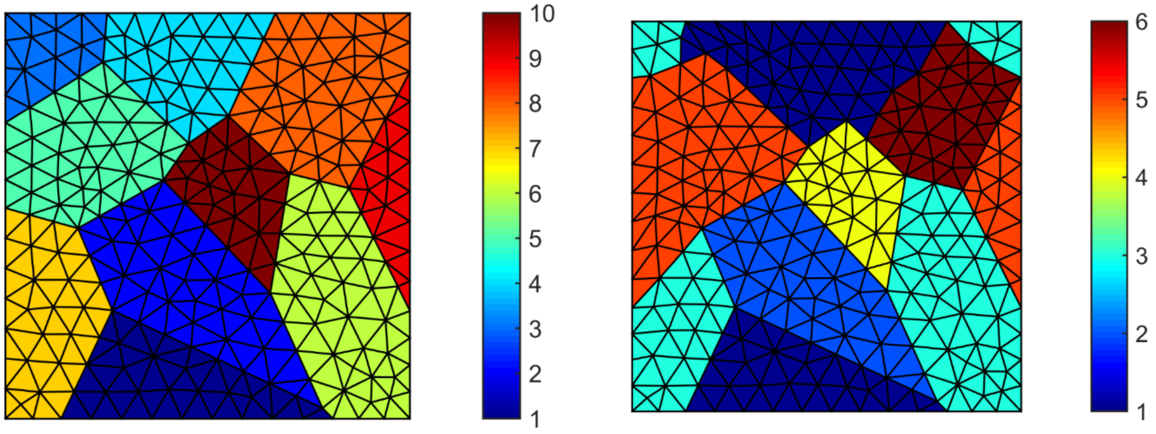

(a) (b)

Figure 13. Two-dimensional RVE with color indicating the grain ID: (a) non-periodic microstructure containing 10 grains; (b) periodic microstructure containing 6 grains

Next, the grain ID and nodes at the top and left edges are adjusted to produce a 6-grain-periodic microstructure containing 466 constant strain triangular (CST) elements and 263 nodes in Figure 13 (b). Notice that the nodes, elements, and grains in the bottom-right section of the RVE are preserved between the original and modified microstructures. A list of the Young's moduli and

Poisson's ratios for the elastic material assigned to each grain is listed in Table 4. Note that the materials are not permitted to yield and thus the problem is hypothetical; however, this problem tests the VMDG method under large strains and material mismatch. The RVE problem is modeled in a finite strain context, and the microstructure is subjected to 50% tensile average strain using deformation gradient $\bar{\boldsymbol{F}}_{\mathrm{M}}$ in (59) applied over 20 equally spaced increments.

$$\bar{\boldsymbol{F}}_{\mathrm{M}} = \begin{bmatrix} 1.0 & 0 \\ 0 & 1.5 \end{bmatrix} \tag{59}$$

Table 4. Material properties of the grains in the RVE

Grains IDs	1	2	3	4	5	6
Elastic modulus (GPA)	101	200	73.1	85	120	80
Poisson's ratio	0.35	0.32	0.35	0.27	0.36	0.28

The contour plots of the stress and displacement results from the VMDG formulation are first presented in Figure 14 and Figure 15, followed by comparing the methods belonging to the VMDG family. The stress and displacement contour plots show that the maximum stress and displacement are $17\,\mathrm{MPa}$ and $0.1\,\mathrm{mm}$. Higher stress values are observed in grains 1, 2, and 5 that form a chain of stiffer grains along the direction of the applied axial strain. Stress gradients appear near the grain boundaries, although a finer mesh would be needed to resolve the features more clearly [60]. A larger instantiation of the 6-grain microstructure shown in Figure 15 (a) is obtained by duplication and translation. The transformed displacement contour plot in Figure 15 (b) shows that the displacement field u_y of the smaller RVE from Figure 14 (b) corresponds with its location within the larger RVE similar to [43], confirming that the computed displacement field is periodic.

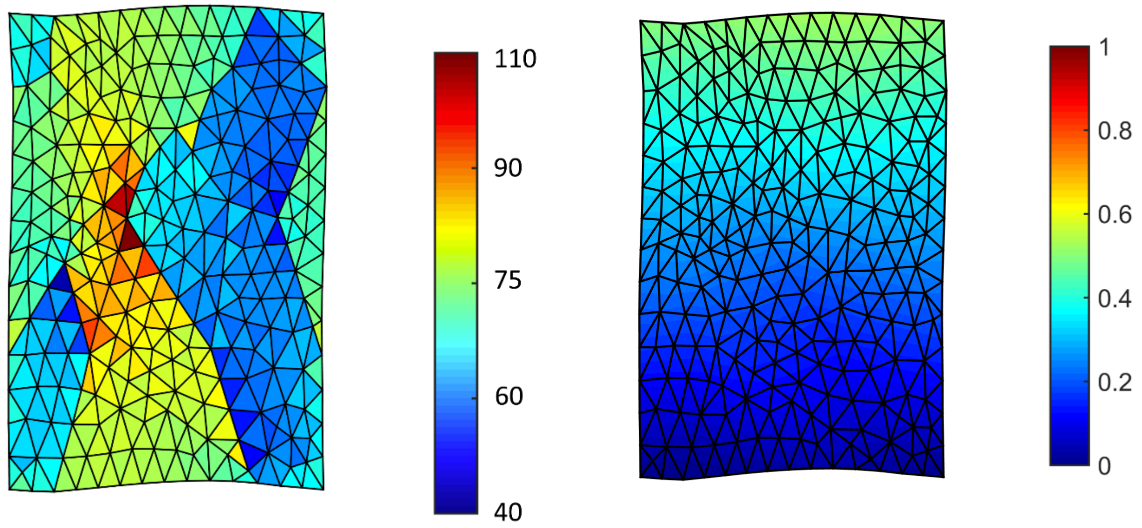

(a) (b)

Figure 14. Solution fields on deformed configuration: (a) tensile stress σ_{yy} (MPa); (b) displacement u_y (mm)

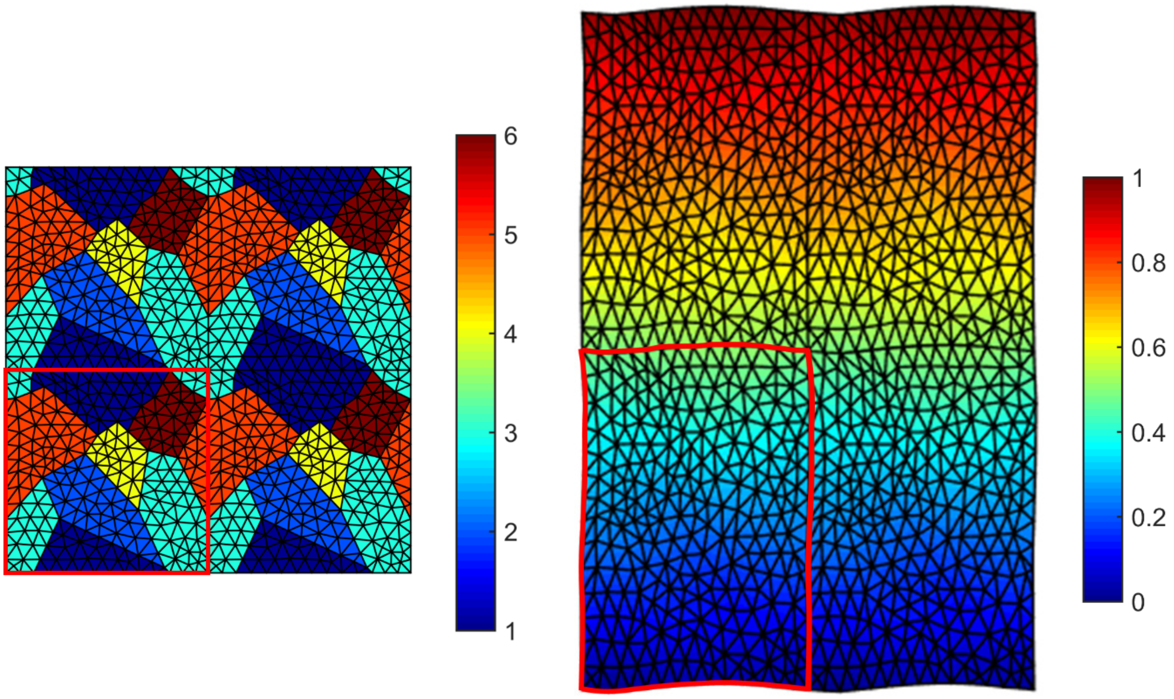

(a) (b)

Figure 15. Larger RVE instantiation: (a) consisting of six repeating grains; (b) displacement u_y contour plot on deformed configuration ×5

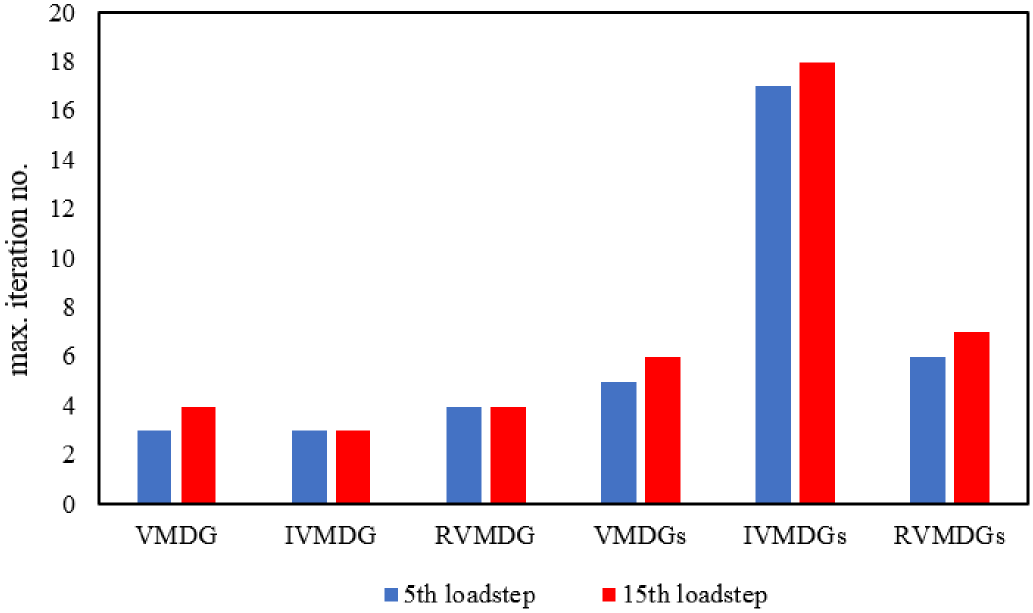

Figure 16. Number of Newton-Raphson iterations for each method at 25% and 75% load level

Computational cost is an important consideration for method development at finite strain. A key driver of cost is the number of Newton iterations, reflecting the number of times the stiffness matrix is formed and factorized. Therefore, each method from the VMDG family is applied to model this RVE, and the number of iterations required to reach a relative convergence tolerance of 4×10^{-14} at the 5th and 15th load steps are presented in Figure 16. The overall trends for the larger and smaller iteration counts match with those observed in [51] for the VMDG method applied to interfaces and discontinuous interpolations. Only 3 or 4 iterations are required by the VMDG, IVMDG, and RVMDG methods, although the load amplitude is small. Thus, choosing between these methods is governed by accuracy and adjoint consistency as discussed next, as well as noting that IVMDG and RVMDG have non-symmetric tangent matrices. The symmetrized methods require more iterations to reach the same tolerance than the original methods, though only a mild increase for VMDGs. Adding these few extra iterations may offset the implementation and runtime costs associated with evaluating the sixth-order curvature tensor $\boldsymbol{\Xi}$.

Table 5. Computed average stress $\boldsymbol{P}_M$ from VMDG method family

Methods	Average stress (GPa)
VMDG	$\begin{bmatrix} -55.361 & 0.3789 \\ 0.5750 & -69.422 \end{bmatrix}$
VMDGs	$\begin{bmatrix} -55.361 & 0.3789 \\ 0.5750 & -69.422 \end{bmatrix}$
IVMDG	$\begin{bmatrix} -55.709 & 0.385 \\ 0.5767 & -69.682 \end{bmatrix}$
IVMDGs	$\begin{bmatrix} -55.709 & 0.385 \\ 0.5767 & -69.682 \end{bmatrix}$
RVMDG	$\begin{bmatrix} -55.599 & 0.3636 \\ 0.5516 & -69.498 \end{bmatrix}$
RVMDGs	$\begin{bmatrix} -55.599 & 0.3636 \\ 0.5516 & -69.498 \end{bmatrix}$

The average stress result from modeling the 2-D microstructure using the VMDG family of algorithms are reported in Table 5. All the methods produce $\boldsymbol{P}_{22}$ stresses within 0.1% of each other, and the symmetrized methods give results matching to their original counterparts. This degree of similarity is somewhat expected since the weak discontinuities for this problem are confined only to the RVE surface. Thus, the VMDGs method's balance of accuracy, number of iteration, and reduced implementation cost merit its use for periodic RVE modeling. Overall, these results are consistent with our previous study [51].

6.4. 3-D microstructure containing 100 grains

The final numerical tests evaluate the performance of the VMDG method for enforcing PBC on complex 3-D RVE models. Most existing studies have employed synthetic block-shaped 3-D RVE for multiscale modeling due to their ease for enforcing PBC. However, the truly/self-periodic 3-D RVE model is an instantiation of a synthetic polycrystalline microstructure that is free from artificial slices through grains. Though it is more difficult to enforce PBC on a truly periodic model such as Figure 17, the benefits of using such models, for example to represent grain boundary sliding, can be appealing [43].

A 3-D truly periodic 100-grain microstructure in Figure 17 (a) is generated using Neper 3.1.0. The discretized model contains 36172 linear tetrahedral elements and 8324 nodes. We show that the 1 mm^3 RVE volume is part of a larger periodic microstructure in Figure 17 (b) by translation. The VMDG method is first compared with the classical LM method for nodal constraints described in our previous study [43]. This is followed by another study to examine the robustness of the VMDG method by modeling transversely isotropic materials in 3-D RVE.

6.4.1 Verification against LM nodal constraint method

The 3-D microstructure RVE in Figure 17 is modelled with uniform isotropic elastic properties $\mathrm{E} = 100\,\mathrm{GPa}$ and $\upsilon = 0.25$ in all grains to verify that both the VMDG and LM methods produce constant stress by consistent enforcement of the periodicity of the microstructure. A combination of tension and shear are applied as the macroscale strain $\bar{\boldsymbol{\varepsilon}}_{\mathrm{M}}$ according to (60). Both methods produced a constant tensile stress σ_{xx} of 1200 MPa and maximum displacement of 0.01 mm, and the displacement contours of the two methods in Figure 18 are essentially identical. As further quantification, we evaluated the surface integral of the periodic constraint $[\![\boldsymbol{u}]\!] - \boldsymbol{\varepsilon}_M [\![\boldsymbol{x}]\!]$ from (52) for the VMDG method. Despite the weak enforcement, this integral (evaluated over half of the total surface area $8.1436\,\text{mm}^2$ of the RVE in Figure 17 (a)) is a zero value up to machine precision. These results demonstrate essential agreement between the strong and weak enforcement of the PBC for this complex RVE problem. Recall that the VMDG method has favorable attributes versus the LM method; namely, the VMDG symmetric stiffness matrix has all positive diagonal entries as opposed to the zeros in the extra rows of the LM constraint equations which can only be avoided by direct condensation during assembly, an added implementational hurdle.

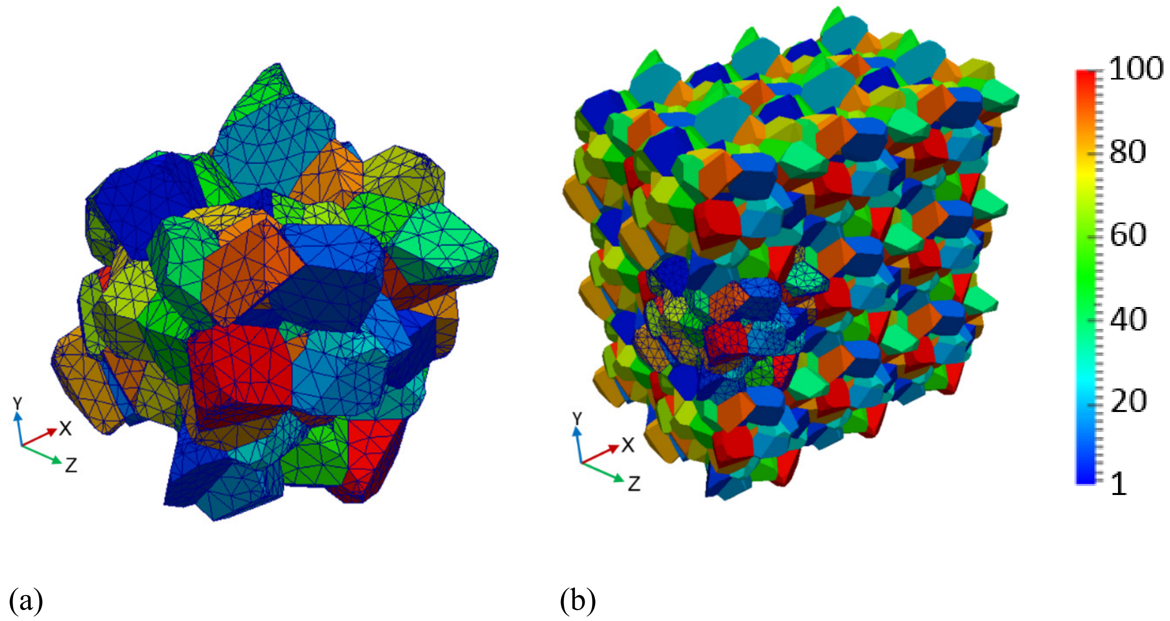

Figure 17. 3-D RVE containing a truly periodic 100-grain microstructure: (a) smaller RVE; (b) larger RVE

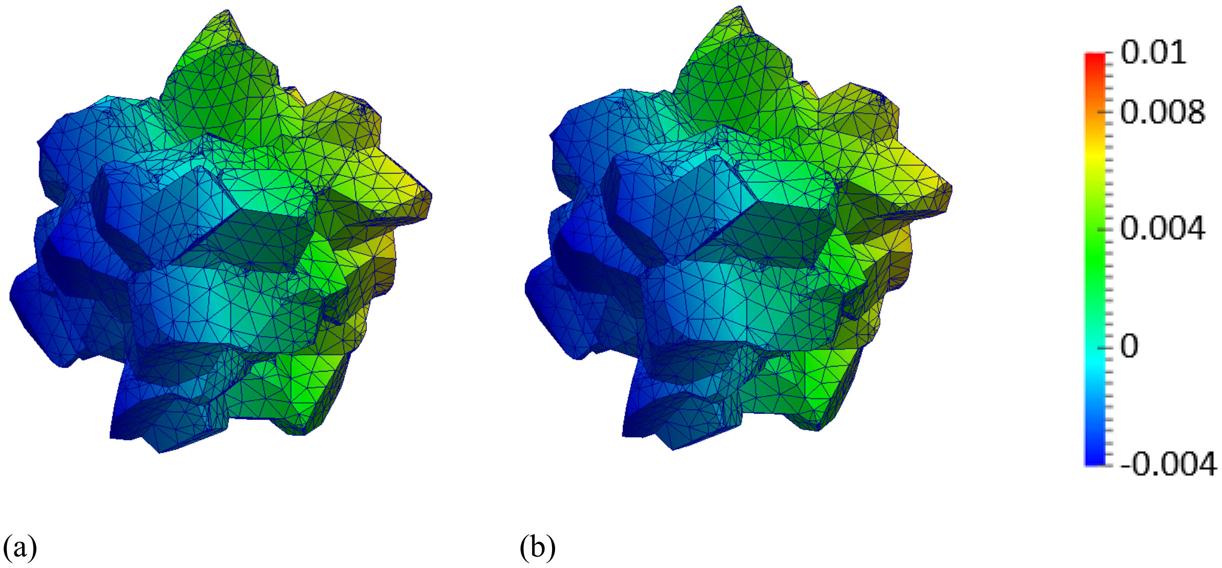

Figure 18. Displacement u_x (mm) on deformed configuration: (a) VMDG method; (b) Lagrange multiplier method

$$\bar{\boldsymbol{\varepsilon}}_{\mathrm{M}} = \begin{bmatrix} 0.01 & 0.01 & 0 \\ 0 & 0 & 0 \\ 0 & 0 & 0 \end{bmatrix} \tag{60}$$

6.4.2 Ti-6Al alloy with transversely isotropic properties

The robustness of the VMDG method is examined herein by modeling a 100-grain microstructure representing a single phase $\alpha-$Ti-6Al alloy. The transversely isotropic elasticity parameters C_{ij} associated to hexagonal close packed $\alpha-$phase titanium at room temperature are taken from [61, 62] as $\mathrm{C}_{11} = \mathrm{C}_{22} = 136\,\mathrm{GPa}$, $\mathrm{C}_{12} = 78\,\mathrm{GPa}$, $\mathrm{C}_{13} = \mathrm{C}_{23} = 68\,\mathrm{GPa}$, $\mathrm{C}_{33} = 163\,\mathrm{GPa}$, $\mathrm{C}_{44} = 29\,\mathrm{GPa}$, $\mathrm{C}_{55} = \mathrm{C}_{66} = 40\,\mathrm{GPa}$ and all other $C_{ij}\text{'}s = 0$. Two orientation distribution functions (ODF), a weak (random) ODF and a strong (fiber) ODF, were generated using MTEX [63] to represent the probability of finding a given lattice orientation within a reference volume. Two statistical samples of 100 orientations were taken from each ODF to provide four instantiations of Ti-6Al texture that are characterized using the pole figures in Figure 19. The Kocks Euler angles from each orientation are then used to transform the transversely isotropic stiffness tensor in the lattice coordinate frame into the global coordinate frame, and that transformed stiffness tensor is assigned to all finite elements of the grain with the associated orientation. Subsequently, the macro and micro scale mechanical response of these RVEs is examined for the two down-samplings of the two different ODF.

The four RVEs are subjected to the same imposed strain defined in (60), and the computed local tensile stress fields are plotted in Figure 20. Gradients in stress are now present within many of the grains as compared to the uniform stress in the previous section. In general, the local stress in each grain is a function of its transformed stiffness tensor as well as the stresses in its surrounding grains. The maximum local tensile stress σ_{xx} in each texture respectively is 150.3 MPa, 186 MPa, 142.8 MPa, and 148.6 MPa and the minimum local tensile stress σ_{xx} in each texture is 87.2 MPa, 64 MPa, 125.2 MPa, and 123.8 MPa. The differing positions of these maximum and minimum values within the microstructure may be connected with the difference in misorientation across the grain boundaries. Since the misorientation between grains is generally larger in the weak texture than the strong texture case, higher stress concentrations are expected and indeed occur in the weak texture models. Note that the behavior herein is elastic; response due to crystal plasticity may not follow this trend.

Texture 1	Texture 2	Texture 3	Texture 4

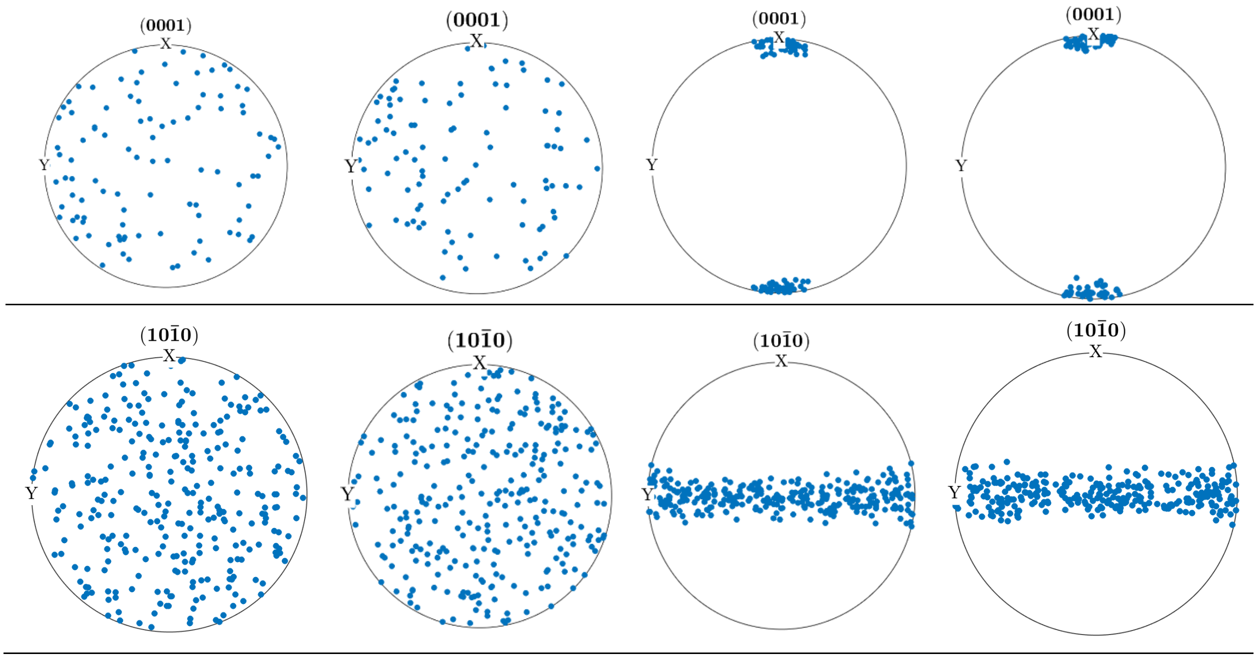

Figure 19. Pole figures for instantiated random and fiber textures of $\alpha-$Ti-6Al alloy

The macroscopic Cauchy stress tensor $\boldsymbol{\sigma}_M$ is listed for all four textures in Table 6. In contrast to the local stress variations, the volume average stresses are fairly close for the two discrete textures from the same ODF, with a relative difference in the σ_{xx} component of less than 0.7%. This behavior is expected since the homogenized stiffness for RVE of polycrystalline elastic materials having the same ODF converges rather quickly with higher number of grains [2, 64, 65], though this convergence typically requires more than 100 grains. However, the homogenized stress from the strong texture cases is noticeably different from the weak texture cases in Table 6, large enough to be attributed to the difference in the underlying ODF. Indeed, the slightly larger σ_{xx} stress for the strong texture case may be associated with the alignment of most grains' [0001] axis with the loading *x*-direction as opposed to the less stiff response of the weak texture case. Additionally, the surface integral of the displacement periodic constraint (52) is reported in the third column of Table 6 for each RVE; note as before that a zero value of the integral means that the error in the PBC is zero. Similar textures produced periodic constraint values that are close to each other. Though these values are all small relative to the $8.1436\,\mathrm{mm}^2$ surface area, the lower value in the strong texture case may be attributed to the expected higher accuracy of the solution with lesser stress gradients compared to the weak texture case. Hence, for this problem with mismatched elastic properties across grain boundaries and others with large applied strain and nonconforming meshes, the VMDG provides accurate weak enforcement of the PBC such that it can reliably provide the homogenized mechanical response and capture interesting features of microscale problems.

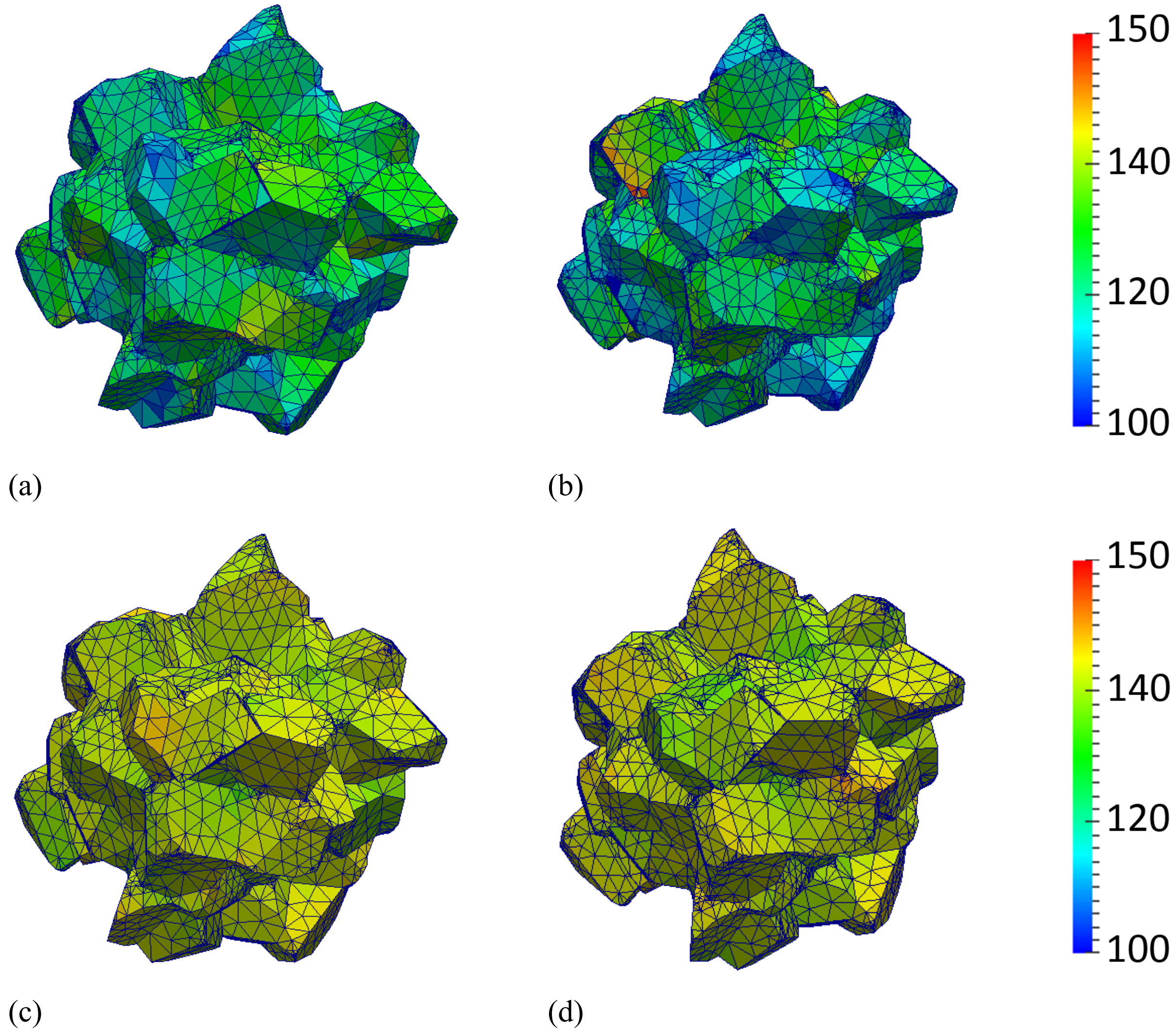

Figure 20. Tensile stress σ_{xx} (MPa) on the deformed configuration: (a) texture 1; (b) texture 2; (c) texture 3; (d) texture 4

Table 6. Volume average stress computed for the titanium textures

	Average stress (MPa)	Periodic constraint
Texture 1	$\begin{bmatrix} -120.1307 & -30.6514 & -0.2487 \\ -30.6514 & -58.5810 & 0.2088 \\ -0.2487 & 0.2088 & -60.6220 \end{bmatrix}$	2.13334×10^{-7} mm^3
Texture 2	$\begin{bmatrix} -119.3662 & -30.5088 & -0.3757 \\ -30.5088 & -60.0456 & 0.5832 \\ -0.3757 & 0.5832 & -59.9275 \end{bmatrix}$	2.02474×10^{-7} mm^3
Texture 3	$\begin{bmatrix} -136.1784 & -33.1791 & -0.4446 \\ -33.1791 & -56.7330 & -0.3572 \\ -0.4446 & -0.3572 & -56.8308 \end{bmatrix}$	5.99651×10^{-8} mm^3
Texture 4	$\begin{bmatrix} -135.2728 & -33.2870 & -0.0636 \\ -33.2870 & -56.8135 & -0.0235 \\ -0.0636 & -0.0235 & -56.7669 \end{bmatrix}$	6.56123×10^{-8} mm^3

7. Conclusions

This paper derives a stabilized DG method from an underlying LM formulation of a periodic microscale boundary value problem by relying on variational multiscale (VMS) ideas. While existing methods for periodic constraints of multiscale problems typically only permit the macro-strain to drive the microscale problem, the rigorous derivation of the VMDG method provides a framework to accommodate either the macro-stress or macro-strain to drive the RVE response. The novelty of the method essentially derives from the idea of imposing the product of the macro-strain times the domain diameter as a non-zero displacement jump within the DG terms on the RVE surfaces. The method does not require solving for additional unknown fields as in mortar-type methods and does not encounter stability concerns that can arise when selecting the function space of the Lagrange multiplier field [18-20]. The method is suited toward enforcing PBC on periodic or non-periodic meshes by partitioning the elements along the boundary surface and representing the fine-scale displacement with bubble functions on sectors. Instead of focusing on only small or finite deformations, the VMDG method is developed in the finite deformation context and subsequently specialized to small deformation of RVEs. Several algorithmic modifications of the method are proposed to provide tradeoffs between variational consistency, algorithmic consistency, adjoint consistency and tangent symmetry.

Several numerical tests confirm the features of the VMDG method. Convergence rate studies on a rectangular composite block evaluate the displacement error in the L_2 norm and H^1 semi norm using different element types. While the linear elements converge optimally, the quadratic elements exhibit suboptimal convergence due to the sharp corners of the inclusions. Next, an RVE with circular voids is loaded by a finite shear strain to compare the performance of the VMDG method for periodic and non-periodic meshes. The resultant macroscale shear stress is found to match closely with values obtained from a reference mortar method for PBC and to not depend on the conformity of the boundary mesh. The consistent linearization of the VMDG method was also verified numerically. Both the rectangular inclusion and circular void problems exhibit convergence of the macroscale stress versus strain response with mesh refinement. The third numerical problem uses a polycrystalline 2-D microstructure to probe the accuracy and computational cost of various members of the VMDG algorithmic family. All variants of the family captured the PBC correctly and produced very similar average stress results. The changes in computational cost (time and memory) arise due to dropping certain boundary terms in the residual vector or tangent matrix. One attractive balance is struck by the VMDGs method which avoids evaluating the sixth order curvature tensor of material moduli, while the IVMDG method possesses the fewest terms and a non-symmetric tangent matrix. Lastly, the VMDG method is used to model a complex 3-dimensional self-periodic RVE containing first isotropic and then anisotropic materials. The former case with uniform material properties confirms that the weakly enforced PBC through the VMDG method produced the same stress and displacement results as the strongly enforced PBC by the LM method. The latter case models consisting of samples of weak and strong textures of a single phase $\alpha-$Ti-6Al alloy within a 100-grain microstructure showed that all textures produced very small errors in the periodic constraint although the error values differed between textures by about a factor of three. The computed volume average stresses under combined tension and shear strain exhibit only 0.7% relative difference between each instantiation, which is reasonable for RVE with a small number of grains. Local stress gradients and periodic surface constraints are well-resolved by the VMDG method.

Acknowledgements

This material is based upon work supported by the National Science Foundation, USA under Grants No. CMMI-1641054 and No. CMMI-1751591.

Appendix. Consistent Linearization

The consistent linearization of the stabilized formulation is performed herein to produce the tangent matrix required to solve the nonlinear microscale behavior using the Newton-Raphson algorithm. We summarize the linearized form of the interface flux, jumps and material acoustic tensor in (61) – (64). The reader is encouraged to refer to [40] for details regarding the linearization of the interface terms and [56] for bulk terms.

$$\mathrm{D}_{\phi^{(+)}}\left[[\![\boldsymbol{\phi}]\!]\right]\cdot\Delta\boldsymbol{u}^{(+)}+\mathrm{D}_{\phi^{(-)}}\left[[\![\boldsymbol{\phi}]\!]\right]\cdot\Delta\boldsymbol{u}^{(-)}=[\![\Delta\boldsymbol{u}]\!] \tag{61}$$

$$\mathrm{D}_{\phi^{(+)}}\left[\left\{\boldsymbol{P}\cdot\boldsymbol{N}\right\}\right]\cdot\Delta\boldsymbol{u}^{(+)}+\mathrm{D}_{\phi^{(-)}}\left[\left\{\boldsymbol{P}\cdot\boldsymbol{N}\right\}\right]\cdot\Delta\boldsymbol{u}^{(-)}=\left\{\left(\mathbf{A}:\mathrm{GRAD}\,\Delta\boldsymbol{u}\right)\cdot\boldsymbol{N}\right\} \tag{62}$$

$$\mathrm{D}_{\phi^{(\alpha)}}\left[\mathbf{A}\right]\cdot\Delta\boldsymbol{u}^{(\alpha)}=\boldsymbol{\Xi}^{(\alpha)}:\mathrm{GRAD}\,\Delta\boldsymbol{u}^{(\alpha)} \tag{63}$$

$$\mathrm{D}_{F_M}\left[\boldsymbol{F}_{\mathrm{M}}[\![\boldsymbol{X}]\!]\right]\cdot\Delta\boldsymbol{\varepsilon}_{\mathrm{M}}=\Delta\boldsymbol{\varepsilon}_{\mathrm{M}}[\![\boldsymbol{X}]\!] \tag{64}$$

For brevity, we show the key steps involved in the linearization procedure for deriving the tangent stiffness associated with the interface terms. We then present for the first time the tangent stiffness associated with the periodic domain boundaries. The integrals will be evaluated by numerical quadrature segment-wise over the union $\bigcup_s \gamma_s = \Gamma^+$.

The first contribution is obtained by linearizing the residual $R(\boldsymbol{\eta}_o;\boldsymbol{\phi})$ using the directional derivative D_{ϕ}:

$$
\begin{aligned}
K_{\boldsymbol{\eta}_o;\boldsymbol{\phi}} &= K(\boldsymbol{\eta}_o, \Delta\boldsymbol{u};\boldsymbol{\phi}) = \mathrm{D}_{\phi^{(\alpha)}}\left[R(\boldsymbol{\eta}_o,\boldsymbol{\phi})\right]\cdot\Delta\boldsymbol{u}^{(\alpha)} \\
&= \int_{\gamma_s} \llbracket \boldsymbol{\eta}_o \rrbracket \cdot \boldsymbol{\tau}_s \cdot \left(\mathrm{D}_{\phi^{(+)}}\left[\llbracket\boldsymbol{\phi}\rrbracket\right]\cdot\Delta\boldsymbol{u}^{(+)} + \mathrm{D}_{\phi^{(-)}}\left[\llbracket\boldsymbol{\phi}\rrbracket\right]\cdot\Delta\boldsymbol{u}^{(-)} \right) \mathrm{d}A \\
&\quad - \int_{\gamma_s} \llbracket \boldsymbol{\eta}_o \rrbracket \cdot \left(\mathrm{D}_{\phi^{(+)}}\left[\{\boldsymbol{P}\cdot\boldsymbol{N}\}\right]\cdot\Delta\boldsymbol{u}^{(+)} + \mathrm{D}_{\phi^{(-)}}\left[\{\boldsymbol{P}\cdot\boldsymbol{N}\}\right]\cdot\Delta\boldsymbol{u}^{(-)} \right) \mathrm{d}A \\
&\quad - \int_{\gamma_s} \left\{ (\mathrm{GRAD}\,\boldsymbol{\eta}_o : \mathsf{A})\cdot\boldsymbol{N} \right\} \cdot \left(\mathrm{D}_{\phi^{(+)}}\left[\llbracket\boldsymbol{\phi}\rrbracket\right]\cdot\Delta\boldsymbol{u}^{(+)} + \mathrm{D}_{\phi^{(-)}}\left[\llbracket\boldsymbol{\phi}\rrbracket\right]\cdot\Delta\boldsymbol{u}^{(-)} \right) \mathrm{d}A \\
&\quad - \int_{\gamma_s} \left\{ \left(\mathrm{GRAD}\,\boldsymbol{\eta}_o : \left(\mathrm{D}_{\phi^{(+)}}\left[\mathsf{A}\right]\cdot\Delta\boldsymbol{u}^{(+)} + \mathrm{D}_{\phi^{(-)}}\left[\mathsf{A}\right]\cdot\Delta\boldsymbol{u}^{(-)} \right) \right)\cdot\boldsymbol{N} \right\} \cdot \left(\llbracket\boldsymbol{\phi}\rrbracket - \boldsymbol{F}_{\mathrm{M}}\llbracket\boldsymbol{X}\rrbracket \right) \mathrm{d}A
\end{aligned}
\tag{65}
$$

The substitution of the linearized forms into (65) yields the final linearized tangent stiffness $K_{\boldsymbol{\eta}_o;\boldsymbol{\phi}}$ for the interface:

$$
\begin{aligned}
K_{\boldsymbol{\eta}_o;\boldsymbol{\phi}} = &\underbrace{\int_{\gamma_s} \llbracket \boldsymbol{\eta}_o \rrbracket \cdot \boldsymbol{\tau}_s \cdot \llbracket \Delta\boldsymbol{u} \rrbracket \,\mathrm{d}A}_{K1} \\
&\underbrace{- \int_{\gamma_s} \llbracket \boldsymbol{\eta}_o \rrbracket \cdot \left\{ (\mathsf{A} : \mathrm{GRAD}\,\Delta\boldsymbol{u})\cdot\boldsymbol{N} \right\} \mathrm{d}A}_{K2} \underbrace{- \int_{\gamma_s} \left\{ (\mathrm{GRAD}\,\boldsymbol{\eta}_o : \mathsf{A})\cdot\boldsymbol{N} \right\} \cdot \llbracket \Delta\boldsymbol{u} \rrbracket \,\mathrm{d}A}_{K3} \\
&\underbrace{- \int_{\gamma_s} \left\{ (\mathrm{GRAD}\,\boldsymbol{\eta}_o : \boldsymbol{\Xi} : \mathrm{GRAD}\,\Delta\boldsymbol{u})\cdot\boldsymbol{N} \right\} \cdot \left(\llbracket\boldsymbol{\phi}\rrbracket - \boldsymbol{F}_{\mathrm{M}}\llbracket\boldsymbol{X}\rrbracket \right) \mathrm{d}A}_{K4}
\end{aligned}
\tag{66}
$$

where the curvature tensor $\boldsymbol{\Xi}(\boldsymbol{F})$ is a sixth-order tensor of material moduli defined as:

$$
\boldsymbol{\Xi}(\boldsymbol{F}) = \frac{\partial^3 W}{\partial\boldsymbol{F}\,\partial\boldsymbol{F}\,\partial\boldsymbol{F}}
\tag{67}
$$

Additionally, the tangent stiffness $K_{\boldsymbol{\eta}_o;\boldsymbol{F}_{\mathrm{M}}}$ is obtained by linearizing the residual $R(\boldsymbol{\eta}_o;\boldsymbol{F}_{\mathrm{M}})$ using the directional derivative $\mathrm{D}_{\boldsymbol{F}_{\mathrm{M}}}$:

$$
\begin{aligned}
K_{\boldsymbol{\eta}_o;\boldsymbol{F}_\mathrm{M}} &= K\left(\boldsymbol{\eta}_o,\Delta\boldsymbol{\varepsilon}_\mathrm{M};\boldsymbol{F}_\mathrm{M}\right)=\mathrm{D}_{\boldsymbol{F}_\mathrm{M}}\left[R\left(\boldsymbol{\eta}_o;\boldsymbol{F}_\mathrm{M}\right)\right]\cdot\Delta\boldsymbol{\varepsilon}_\mathrm{M}\\
&=\int_{\gamma_s}[\![\boldsymbol{\eta}_o]\!]\cdot\boldsymbol{\tau}_s\cdot\left(\mathrm{D}_{\boldsymbol{F}_\mathrm{M}}\left[-\boldsymbol{F}_\mathrm{M}[\![\boldsymbol{X}]\!]\right]\cdot\Delta\boldsymbol{\varepsilon}_\mathrm{M}\right)\mathrm{d}A\\
&-\int_{\gamma_s}\left\{\left(\mathrm{GRAD}\,\boldsymbol{\eta}_o:\mathbf{A}\right)\cdot\boldsymbol{N}\right\}\cdot\left(\mathrm{D}_{\boldsymbol{F}_\mathrm{M}}\left[-\boldsymbol{F}_\mathrm{M}[\![\boldsymbol{X}]\!]\right]\cdot\Delta\boldsymbol{\varepsilon}_\mathrm{M}\right)\mathrm{d}A
\end{aligned}
\tag{68}
$$

The substitution of the linearization (64) into (68) yields the final linearized tangent stiffness $K_{\boldsymbol{\eta}_o;\boldsymbol{F}_\mathrm{M}}$ in (69).

$$
K_{\boldsymbol{\eta}_o;\boldsymbol{F}_\mathrm{M}}=\underbrace{-\int_{\gamma_s}[\![\boldsymbol{\eta}_o]\!]\cdot\boldsymbol{\tau}_s\cdot\Delta\boldsymbol{\varepsilon}_\mathrm{M}[\![\boldsymbol{X}]\!]\,\mathrm{d}A}_{K1}+\underbrace{\int_{\gamma_s}\left\{\left(\mathrm{GRAD}\,\boldsymbol{\eta}_o:\mathbf{A}\right)\cdot\boldsymbol{N}\right\}\cdot\Delta\boldsymbol{\varepsilon}_\mathrm{M}[\![\boldsymbol{X}]\!]\,\mathrm{d}A}_{K3}
\tag{69}
$$

The tangent stiffness $K_{\boldsymbol{\kappa};\boldsymbol{\phi}}$ is obtained by linearizing the residual $R\left(\boldsymbol{\kappa};\boldsymbol{\phi}\right)$ using the directional derivative D_{ϕ}:

$$
\begin{aligned}
K_{\boldsymbol{\kappa};\boldsymbol{\phi}} &= K\left(\boldsymbol{\kappa},\Delta\boldsymbol{u};\boldsymbol{\phi}\right)=\mathrm{D}_{\phi^{(\alpha)}}\left[R\left(\boldsymbol{\kappa};\boldsymbol{\phi}\right)\right]\cdot\Delta\boldsymbol{u}^{(\alpha)}\\
&=-\int_{\gamma_s}\boldsymbol{\kappa}[\![\boldsymbol{X}]\!]\cdot\boldsymbol{\tau}_s\cdot\left(\mathrm{D}_{\phi^{(+)}}\left[[\![\boldsymbol{\phi}]\!]\right]\cdot\Delta\boldsymbol{u}^{(+)}+\mathrm{D}_{\phi^{(-)}}\left[[\![\boldsymbol{\phi}]\!]\right]\cdot\Delta\boldsymbol{u}^{(-)}\right)\mathrm{d}A\\
&+\int_{\gamma_s}\boldsymbol{\kappa}[\![\boldsymbol{X}]\!]\cdot\left(\mathrm{D}_{\phi^{(+)}}\left[\left\{\boldsymbol{P}\cdot\boldsymbol{N}\right\}\right]\cdot\Delta\boldsymbol{u}^{(+)}+\mathrm{D}_{\phi^{(-)}}\left[\left\{\boldsymbol{P}\cdot\boldsymbol{N}\right\}\right]\cdot\Delta\boldsymbol{u}^{(-)}\right)\mathrm{d}A
\end{aligned}
\tag{70}
$$

The substitution of the linearized forms into (70) yields:

$$
K_{\boldsymbol{\kappa};\boldsymbol{\phi}}=\underbrace{-\int_{\gamma_s}\boldsymbol{\kappa}[\![\boldsymbol{X}]\!]\cdot\boldsymbol{\tau}_s\cdot[\![\Delta\boldsymbol{u}]\!]\,\mathrm{d}A}_{K1}+\underbrace{\int_{\gamma_s}\boldsymbol{\kappa}[\![\boldsymbol{X}]\!]\cdot\left\{\left(\mathbf{A}:\mathrm{GRAD}\,\Delta\boldsymbol{u}\right)\cdot\boldsymbol{N}\right\}\mathrm{d}A}_{K2}
\tag{71}
$$

The tangent stiffness $K_{\boldsymbol{\kappa};\boldsymbol{F}_\mathrm{M}}$ is obtained by linearizing the residual $R\left(\boldsymbol{\kappa};\boldsymbol{F}_\mathrm{M}\right)$ using the directional derivative $\mathrm{D}_{\boldsymbol{F}_\mathrm{M}}$:

$$
\begin{aligned}
K_{\boldsymbol{\kappa};\boldsymbol{F}_\mathrm{M}} &= K\left(\boldsymbol{\kappa},\Delta\boldsymbol{\varepsilon}_\mathrm{M};\boldsymbol{F}_\mathrm{M}\right)=\mathrm{D}_{\boldsymbol{F}_\mathrm{M}}\left[R\left(\boldsymbol{\kappa};\boldsymbol{F}_\mathrm{M}\right)\right]\cdot\Delta\boldsymbol{\varepsilon}_\mathrm{M}\\
&=-\int_{\gamma_s}[\![\boldsymbol{\kappa}]\!]\cdot\boldsymbol{\tau}_s\cdot\left(\mathrm{D}_{\boldsymbol{F}_\mathrm{M}}\left[-\boldsymbol{F}_\mathrm{M}[\![\boldsymbol{X}]\!]\right]\cdot\Delta\boldsymbol{\varepsilon}_\mathrm{M}\right)\mathrm{d}A
\end{aligned}
\tag{72}
$$

The substitution of the linearization (69) into (72) yields the final tangent stiffness:

$$
K_{\boldsymbol{\kappa};\boldsymbol{F}_\mathrm{M}}=\underbrace{\int_{\gamma_s}\boldsymbol{\kappa}[\![\boldsymbol{X}]\!]\cdot\boldsymbol{\tau}_s\cdot\Delta\boldsymbol{\varepsilon}_\mathrm{M}[\![\boldsymbol{X}]\!]\,\mathrm{d}A}_{K1}
\tag{73}
$$

Notice that the tangent stiffness is symmetric with respect to its arguments because $K_{\boldsymbol{\eta}_o;\boldsymbol{\phi}}\left(\boldsymbol{\eta}_o, \Delta\boldsymbol{u}\right) = K_{\boldsymbol{\eta}_o;\boldsymbol{\phi}}\left(\Delta\boldsymbol{u}, \boldsymbol{\eta}_o\right)$, $K_{\boldsymbol{\eta}_o;\boldsymbol{F}_{\mathrm{M}}}\left(\boldsymbol{\eta}_o, \Delta\boldsymbol{\varepsilon}_{\mathrm{M}}\right) = K_{\boldsymbol{\kappa};\boldsymbol{\phi}}\left(\Delta\boldsymbol{\varepsilon}_{\mathrm{M}}, \boldsymbol{\eta}_o\right)$, and $K_{\boldsymbol{\kappa};\boldsymbol{F}_{\mathrm{M}}}\left(\boldsymbol{\kappa}, \Delta\boldsymbol{\varepsilon}_{\mathrm{M}}\right) = K_{\boldsymbol{\kappa};\boldsymbol{F}_{\mathrm{M}}}\left(\Delta\boldsymbol{\varepsilon}_{\mathrm{M}}, \boldsymbol{\kappa}\right)$, which is expected due to the existence of the potential functional (23).

The VMDG formulation can be straightforwardly implemented into standard pure-displacement finite element codes by discretizing the four linearized forms with shape functions, converting to matrix form, grouping the $(+)$ terms together and the $(-)$ terms together, and carefully arranging the resulting sub-matrices into a total element stiffness matrix (74).

$$K_{\boldsymbol{\eta}_o;\boldsymbol{\phi}}\left(\boldsymbol{\eta}_o^h, \Delta\boldsymbol{u}^h\right) + K_{\boldsymbol{\eta}_o;\boldsymbol{F}_{\mathrm{M}}}\left(\boldsymbol{\eta}_o^h, \Delta\boldsymbol{\varepsilon}_{\mathrm{M}}^h\right) + K_{\boldsymbol{\kappa};\boldsymbol{\phi}}\left(\boldsymbol{\kappa}^h, \Delta\boldsymbol{u}^h\right) + K_{\boldsymbol{\kappa};\boldsymbol{F}_{\mathrm{M}}}\left(\boldsymbol{\kappa}^h, \Delta\boldsymbol{\varepsilon}_{\mathrm{M}}^h\right) = \mathbf{W}^T\mathbf{K}\mathbf{U} \tag{74}$$

$$\mathbf{K} = \begin{bmatrix} \mathbf{K}_{\boldsymbol{\eta}_o;\boldsymbol{\phi}}^{++} & \mathbf{K}_{\boldsymbol{\eta}_o;\boldsymbol{\phi}}^{+-} & \mathbf{K}_{\boldsymbol{\eta}_o;\boldsymbol{F}_{\mathrm{M}}}^{+*} \\ \mathbf{K}_{\boldsymbol{\eta}_o;\boldsymbol{\phi}}^{-+} & \mathbf{K}_{\boldsymbol{\eta}_o;\boldsymbol{\phi}}^{--} & \mathbf{K}_{\boldsymbol{\eta}_o;\boldsymbol{F}_{\mathrm{M}}}^{-*} \\ \mathbf{K}_{\boldsymbol{\kappa};\boldsymbol{\phi}}^{*+} & \mathbf{K}_{\boldsymbol{\kappa};\boldsymbol{\phi}}^{*-} & \mathbf{K}_{\boldsymbol{\kappa};\boldsymbol{F}_{\mathrm{M}}}^{**} \end{bmatrix}, \quad \mathbf{W} = \begin{bmatrix} \mathbf{w}^+ \\ \mathbf{w}^- \\ \boldsymbol{\kappa}^* \end{bmatrix}, \quad \mathbf{U} = \begin{bmatrix} \mathbf{u}^+ \\ \mathbf{u}^- \\ \boldsymbol{\varepsilon}^* \end{bmatrix} \tag{75}$$

The further decomposition of $\mathbf{K}$ into $(+)$, $(-)$ and $(*)$ components is analogous to the decomposed interface stiffness matrix for the discontinuous Galerkin method presented in [39]. Taking for example the linear quadrilateral element mentioned in Section 3.3, the vector $\mathbf{u}^+$ contains the x and y degrees of freedom for the four nodes of the element Ω_e^+ containing the sector ω_s^+ adjacent to γ_s, vector $\mathbf{u}^-$ contains the eight degrees of freedom from element Ω_e^-, and $\boldsymbol{\varepsilon}$ contains the x and y degrees of freedom for the two "macro" nodes of the RVE.

Notice that the all derivations herein are done in the reference configuration. Similar to [40], this method could be easily implemented in the current configuration. The reader is referred to the appendix of [40] for details.

References

1. Eshelby, J.D., *The determination of the elastic field of an ellipsoidal inclusion, and related problems.* Proceedings of the Royal Society of London. Series A. Mathematical and Physical Sciences, 1957. **241**(1226): p. 376-396.
2. Nemat-Nasser, S. and M. Hori, *Micromechanics: overall properties of heterogeneous materials*. Vol. 37. 2013: Elsevier.
3. Goudarzi, T. and O. Lopez-Pamies, *Numerical modeling of the nonlinear elastic response of filled elastomers via composite-sphere assemblages.* Journal of Applied Mechanics, 2013. **80**(5): p. 050906.
4. Li, Y., et al., *Analytical homogenization for stretch and bending of honeycomb sandwich plates with skin and height effects.* Composite Structures, 2015. **120**: p. 406-416.
5. Miehe, C. and A. Koch, *Computational micro-to-macro transitions of discretized microstructures undergoing small strains.* Archive of Applied Mechanics, 2002. **72**(4-5): p. 300-317.
6. Terada, K., et al., *Simulation of the multi-scale convergence in computational homogenization approaches.* International Journal of Solids and Structures, 2000. **37**(16): p. 2285-2311.
7. Geers, M.G., V.G. Kouznetsova, and W. Brekelmans, *Multi-scale computational homogenization: Trends and challenges.* Journal of computational and applied mathematics, 2010. **234**(7): p. 2175-2182.
8. Nguyen, V.-D., et al., *Imposing periodic boundary condition on arbitrary meshes by polynomial interpolation.* Computational Materials Science, 2012. **55**: p. 390-406.
9. Michel, J.-C., H. Moulinec, and P. Suquet, *Effective properties of composite materials with periodic microstructure: a computational approach.* Computer methods in applied mechanics and engineering, 1999. **172**(1-4): p. 109-143.
10. Kouznetsova, V., M. Geers, and W. Brekelmans, *Multi-scale second-order computational homogenization of multi-phase materials: a nested finite element solution strategy.* Computer Methods in Applied Mechanics and Engineering, 2004. **193**(48-51): p. 5525-5550.
11. Miehe, C., J. Schotte, and J. Schröder, *Computational micro–macro transitions and overall moduli in the analysis of polycrystals at large strains.* Computational Materials Science, 1999. **16**(1-4): p. 372-382.
12. Larsson, F., et al., *Computational homogenization based on a weak format of micro-periodicity for RVE-problems.* Computer Methods in Applied Mechanics and Engineering, 2011. **200**(1-4): p. 11-26.
13. Kanit, T., et al., *Determination of the size of the representative volume element for random*

composites: statistical and numerical approach. International Journal of solids and structures, 2003. **40**(13-14): p. 3647-3679.

14. Miehe, C., *Strain‐driven homogenization of inelastic microstructures and composites based on an incremental variational formulation.* International Journal for numerical methods in engineering, 2002. **55**(11): p. 1285-1322.
15. Geers, M.G., et al., *Homogenization methods and multiscale modeling: Nonlinear problems.* Encyclopedia of Computational Mechanics Second Edition, 2017: p. 1-34.
16. Miehe, C., *Computational micro-to-macro transitions for discretized micro-structures of heterogeneous materials at finite strains based on the minimization of averaged incremental energy.* Computer Methods in Applied Mechanics and Engineering, 2003. **192**(5-6): p. 559-591.
17. Swan, C.C., *Techniques for stress-and strain-controlled homogenization of inelastic periodic composites.* Computer Methods in Applied Mechanics and Engineering, 1994. **117**(3-4): p. 249-267.
18. Reis, F. and F.A. Pires, *A mortar based approach for the enforcement of periodic boundary conditions on arbitrarily generated meshes.* Computer Methods in Applied Mechanics and Engineering, 2014. **274**: p. 168-191.
19. Sanders, J. and M.A. Puso, *An embedded mesh method for treating overlapping finite element meshes.* International Journal for Numerical Methods in Engineering, 2012. **91**(3): p. 289-305.
20. Sanders, J.D., T.A. Laursen, and M.A. Puso, *A Nitsche embedded mesh method.* Computational Mechanics, 2012. **49**(2): p. 243-257.
21. Wohlmuth, B.I., *A mortar finite element method using dual spaces for the Lagrange multiplier.* SIAM journal on numerical analysis, 2000. **38**(3): p. 989-1012.
22. Flemisch, B. and B.I. Wohlmuth, *Stable Lagrange multipliers for quadrilateral meshes of curved interfaces in 3D.* Computer Methods in Applied Mechanics and Engineering, 2007. **196**(8): p. 1589-1602.
23. Popp, A., et al., *Improved robustness and consistency of 3D contact algorithms based on a dual mortar approach.* Computer Methods in Applied Mechanics and Engineering, 2013. **264**: p. 67-80.
24. Monteiro, E., J. Yvonnet, and Q.-C. He, *Computational homogenization for nonlinear conduction in heterogeneous materials using model reduction.* Computational Materials Science, 2008. **42**(4): p. 704-712.
25. Yang, Q.-S. and W. Becker, *Numerical investigation for stress, strain and energy homogenization of orthotropic composite with periodic microstructure and non-symmetric inclusions.* Computational Materials Science, 2004. **31**(1-2): p. 169-180.
26. Zhang, X. and C. Oskay, *Eigenstrain based reduced order homogenization for polycrystalline materials.* Computer Methods in Applied Mechanics and Engineering,

2015. **297**: p. 408-436.

27. Wentorf, R., et al., *Automated modeling for complex woven mesostructures.* Computer Methods in Applied Mechanics and Engineering, 1999. **172**(1-4): p. 273-291.
28. Tyrus, J., M. Gosz, and E. DeSantiago, *A local finite element implementation for imposing periodic boundary conditions on composite micromechanical models.* International Journal of Solids and Structures, 2007. **44**(9): p. 2972-2989.
29. Scovazzi, G., T. Song, and X. Zeng, *A velocity/stress mixed stabilized nodal finite element for elastodynamics: Analysis and computations with strongly and weakly enforced boundary conditions.* Computer Methods in Applied Mechanics and Engineering, 2017. **325**: p. 532-576.
30. Stoter, S.K., et al., *Residual-based variational multiscale modeling in a discontinuous Galerkin framework.* Multiscale Modeling & Simulation, 2018. **16**(3): p. 1333-1364.
31. Markov, S.I. *Multiscale Nonconformal Finite Element Methods for Solving Problems with Moving Boundaries*. in *2018 XIV International Scientific-Technical Conference on Actual Problems of Electronics Instrument Engineering (APEIE)*. 2018. IEEE.
32. Abedi, R. and R.B. Haber, *Spacetime simulation of dynamic fracture with crack closure and frictional sliding.* Advanced Modeling and Simulation in Engineering Sciences, 2018. **5**(1): p. 22.
33. Stoter, S.K., et al., *A discontinuous Galerkin residual‐based variational multiscale method for modeling subgrid‐scale behavior of the viscous Burgers equation.* International Journal for Numerical Methods in Fluids, 2018. **88**(5): p. 217-238.
34. Vemaganti, K., *Discontinuous Galerkin methods for periodic boundary value problems.* Numerical Methods for Partial Differential Equations: An International Journal, 2007. **23**(3): p. 587-596.
35. Nguyen, V.-D., G. Becker, and L. Noels, *Multiscale computational homogenization methods with a gradient enhanced scheme based on the discontinuous Galerkin formulation.* Computer Methods in Applied Mechanics and Engineering, 2013. **260**: p. 63-77.
36. Truster, T.J. and A. Masud, *Primal interface formulation for coupling multiple PDEs: A consistent derivation via the Variational Multiscale method.* Computer Methods in Applied Mechanics and Engineering, 2014. **268**: p. 194-224.
37. Chen, P., T.J. Truster, and A. Masud, *Interfacial stabilization at finite strains for weak and strong discontinuities in multi-constituent materials.* Computer Methods in Applied Mechanics and Engineering, 2018. **328**: p. 717-751.
38. Truster, T.J. and A. Masud, *A discontinuous/continuous Galerkin method for modeling of interphase damage in fibrous composite systems.* Computational Mechanics, 2013. **52**(3): p. 499-514.
39. Aduloju, S.C. and T.J. Truster, *A variational multiscale discontinuous Galerkin*

formulation for both implicit and explicit dynamic modeling of interfacial fracture. Computer Methods in Applied Mechanics and Engineering, 2019. **343**: p. 602-630.

40. Truster, T.J., P. Chen, and A. Masud, *Finite strain primal interface formulation with consistently evolving stabilization.* International Journal for Numerical Methods in Engineering, 2015. **102**(3-4): p. 278-315.
41. Hill, R., *A self-consistent mechanics of composite materials.* Journal of the Mechanics and Physics of Solids, 1965. **13**(4): p. 213-222.
42. Perić, D., et al., *On micro‐to‐macro transitions for multi‐scale analysis of non‐linear heterogeneous materials: unified variational basis and finite element implementation.* International Journal for Numerical Methods in Engineering, 2011. **87**(1‐5): p. 149-170.
43. Aduloju, S.C. and T.J. Truster, *On Topology-based Cohesive Interface Element Insertion along Periodic Boundary Surfaces.* Engineering Fracture Mechanics, 2018.
44. Barbosa, H.J. and T.J. Hughes, *The finite element method with Lagrange multipliers on the boundary: circumventing the Babuška-Brezzi condition.* Computer Methods in Applied Mechanics and Engineering, 1991. **85**(1): p. 109-128.
45. Brezzi, F. and M. Fortin, *Mixed and hybrid finite element methods*. Vol. 15. 2012: Springer Science & Business Media.
46. Hughes, T.J., *Multiscale phenomena: Green's functions, the Dirichlet-to-Neumann formulation, subgrid scale models, bubbles and the origins of stabilized methods.* Computer methods in applied mechanics and engineering, 1995. **127**(1-4): p. 387-401.
47. Masud, A. and T.J. Truster, *A framework for residual-based stabilization of incompressible finite elasticity: Stabilized formulations and F methods for linear triangles and tetrahedra.* Computer Methods in Applied Mechanics and Engineering, 2013. **267**: p. 359-399.
48. Masud, A., T.J. Truster, and L.A. Bergman, *A variational multiscale a posteriori error estimation method for mixed form of nearly incompressible elasticity.* Computer Methods in Applied Mechanics and Engineering, 2011. **200**(47-48): p. 3453-3481.
49. Truster, T.J. and A. Masud, *Discontinuous galerkin method for frictional interface dynamics.* Journal of Engineering Mechanics, 2016. **142**(11): p. 04016084.
50. Truster, T.J., *A stabilized, symmetric Nitsche method for spatially localized plasticity.* Computational Mechanics, 2016. **57**(1): p. 75-103.
51. Truster, T.J., P. Chen, and A. Masud, *On the algorithmic and implementational aspects of a discontinuous Galerkin method at finite strains.* Computers & Mathematics with Applications, 2015. **70**(6): p. 1266-1289.
52. Mergheim, J. and P. Steinmann, *A geometrically nonlinear FE approach for the simulation of strong and weak discontinuities.* Computer Methods in Applied Mechanics and Engineering, 2006. **195**(37-40): p. 5037-5052.
53. Scovazzi, G., et al., *A simple, stable, and accurate linear tetrahedral finite element for transient, nearly, and fully incompressible solid dynamics: a dynamic variational*

multiscale approach. International Journal for Numerical Methods in Engineering, 2016. **106**(10): p. 799-839.

54. Cervera, M., et al., *Mixed linear/linear simplicial elements for incompressible elasticity and plasticity.* Computer Methods in Applied Mechanics and Engineering, 2003. **192**(49): p. 5249-5263.
55. Masud, A. and T.J. Truster, *A framework for residual-based stabilization of incompressible finite elasticity: stabilized formulations and methods for linear triangles and tetrahedra.* Computer Methods in Applied Mechanics and Engineering, 2013. **267**: p. 359-399.
56. Belytschko, T., et al., *Nonlinear finite elements for continua and structures*. 2013: John wiley & sons.
57. Danielsson, M., D. Parks, and M. Boyce, *Three-dimensional micromechanical modeling of voided polymeric materials.* Journal of the Mechanics and Physics of Solids, 2002. **50**(2): p. 351-379.
58. Truster, T.J., *DEIP, discontinuous element insertion Program—Mesh generation for interfacial finite element modeling.* SoftwareX, 2018. **7**: p. 162-170.
59. Quey, R., P. Dawson, and F. Barbe, *Large-scale 3D random polycrystals for the finite element method: Generation, meshing and remeshing.* Computer Methods in Applied Mechanics and Engineering, 2011. **200**(17-20): p. 1729-1745.
60. Nassif, O., et al., *Combined crystal plasticity and grain boundary modeling of creep in ferritic-martensitic steels: I. Theory and implementation.* Modelling and Simulation in Materials Science and Engineering, 2019. **27**(7): p. 075009.
61. Hasija, V., et al., *Deformation and creep modeling in polycrystalline Ti–6Al alloys.* Acta materialia, 2003. **51**(15): p. 4533-4549.
62. Kim, J.-Y., V. Yakovlev, and S. Rokhlin. *Line-focus acoustic microscopy of Ti-6242 α/β single colony: determination of elastic constants*. in *AIP Conference Proceedings*. 2002. AIP.
63. Hielscher, R. and H. Schaeben, *A novel pole figure inversion method: specification of the MTEX algorithm.* Journal of Applied Crystallography, 2008. **41**(6): p. 1024-1037.
64. Kovac, M., I. Simonovski, and L. Cizelj, *Estimating minimum polycrystalline aggregate size for macroscopic material homogeneity.* 2002.
65. Kovač, M. and L. Cizelj, *Modeling elasto-plastic behavior of polycrystalline grain structure of steels at mesoscopic level.* Nuclear engineering and design, 2005. **235**(17-19): p. 1939-1950.